

RESEARCH ARTICLE

10.1002/2013JB010883

Key Points:

- Sharp transition in slab dip observed near abrupt end of volcanic belt
- Seismicity and structural evidence suggests possible tear in S Cocos slab
- Slab tears may play an important role in the rollback process

Supporting Information:

- Readme
- Figure S1
- Figure S2
- Figure S3
- Figure S4
- Figure S5
- Figure S6

Correspondence to:

S. L. Dougherty,
sarad@gps.caltech.edu

Citation:

Dougherty, S. L., and R. W. Clayton (2014), Seismicity and structure in central Mexico: Evidence for a possible slab tear in the South Cocos plate, *J. Geophys. Res. Solid Earth*, 119, 3424–3447, doi:10.1002/2013JB010883.

Received 2 DEC 2013

Accepted 6 APR 2014

Accepted article online 9 APR 2014

Published online 29 APR 2014

Corrected 2 JUL 2014

This article was corrected on 2 JUL 2014. See the end of the full text for details.

Seismicity and structure in central Mexico: Evidence for a possible slab tear in the South Cocos plate

Sara L. Dougherty¹ and Robert W. Clayton¹
¹ Seismological Laboratory, California Institute of Technology, Pasadena, California, USA

Abstract The morphology of the transition from flat to normal subduction in eastern central Mexico is explored using intraslab earthquakes recorded by temporary and permanent regional seismic arrays. Observations of a sharp transition in slab dip near the abrupt end of the Trans-Mexican Volcanic Belt (TMVB) suggest a possible slab tear located within the subducted South Cocos plate. The eastern lateral extent of a thin ultra-slow velocity layer (USL) imaged atop the Cocos slab in recent studies along the Meso America Subduction Experiment array is examined here using additional data. We find an end to this USL which is coincident with the western boundary of a zone of decreased seismicity and the end of the TMVB near the sharp transition in slab dip. Waveform modeling of the 2-D structure in this region using a finite difference algorithm provides constraints on the velocity and geometry of the slab's seismic structure and confirms the location of the USL. Analysis of intraslab seismicity patterns reveals clustering, sudden increase in depth, variable focal mechanism orientations and faulting types, and alignment of source mechanisms along the sharp transition in slab dip. The seismicity and structural evidence suggests a possible tear in the South Cocos slab. This potential tear, together with the tear along the Orozco Fracture Zone to the northwest, indicates a slab rollback mechanism in which separate slab segments move independently, allowing for mantle flow between the segments.

1. Introduction

Slab tears are tectonically important morphological features of subducted plates that have been proposed to occur in numerous subduction zones. These tears can propagate horizontally resulting in lateral slab detachment or vertically, both of which produce observable gaps between slab segments. A slab tear can occur due to subduction of seafloor heterogeneities [e.g., *Bonnardot et al.*, 2009], a transition from subduction to strike-slip motion along the plate boundary [e.g., *Clark et al.*, 2008], along-strike changes in slab geometry [e.g., *Miller et al.*, 2004], lateral variation in slab rollback [e.g., *Govers and Wortel*, 2005], variable plate motion along strike [e.g., *Bandy et al.*, 2000], and/or a change in plate structure, temperature, and/or age [e.g., *Lonsdale*, 2005; *Burkett and Billen*, 2010]. Locations where a slab tear has been suggested include Tonga [*Millen and Hamburger*, 1998; *Bonnardot et al.*, 2009], southern Izu-Bonin arc [*Miller et al.*, 2004], southern Mariana arc [*Fryer et al.*, 2003; *Miller et al.*, 2006], Costa Rica [*Johnston and Thorkelson*, 1997; *Abt et al.*, 2010], western central Mexico [*Dougherty et al.*, 2012; *Stubailo et al.*, 2012], Colombia [*Vargas and Mann*, 2013], Chile [*Cahill and Isacks*, 1992; *Pesicek et al.*, 2012], southern and northern Lesser Antilles [*ten Brink*, 2005; *Clark et al.*, 2008; *Meighan et al.*, 2013a], and the Mediterranean [*Wortel and Spakman*, 2000; *Gasparon et al.*, 2009; *Suckale et al.*, 2009] among others. The occurrence of a possible slab tear can be indicated by observations of seismic anisotropy from SKS splitting directions [e.g., *Peyton et al.*, 2001; *Soto et al.*, 2009], upper plate deformation (e.g., rifting) [e.g., *Yang et al.*, 2009; *Vargas and Mann*, 2013], abrupt changes in Wadati-Benioff zone seismicity [e.g., *Protti et al.*, 1994; *Dougherty et al.*, 2012], focal mechanism orientations [e.g., *Millen and Hamburger*, 1998; *Gutscher et al.*, 1999], seismicity patterns (e.g., clusters or gaps) [e.g., *Miller et al.*, 2004; *Meighan et al.*, 2013b], holes in tomographic images [e.g., *Miller et al.*, 2005; *Pesicek et al.*, 2012], and/or changes in arc volcanism (e.g., composition, orientation, and/or gap) [e.g., *Ferrari*, 2004; *Lin et al.*, 2004].

Tearing of the subducted oceanic lithosphere creates a gap in the plate through which asthenospheric mantle may flow, explaining both observed changes in seismic anisotropy and surface volcanism. The abrupt rotation of trench-parallel SKS fast directions to trench-perpendicular near a slab tear (or a circular pattern of anisotropy around a slab edge) indicates 3-D toroidal flow of mantle material through the gap [*Peyton et al.*, 2001; *Kneller and van Keken*, 2008; *Zandt and Humphreys*, 2008] that has important implications for rollback

of the subducted plate. A tear in the plate would shortcut the trench-parallel flow that occurs beneath the slab as it rolls back, providing a conduit for the transfer of material into the overlying mantle wedge [Russo and Silver, 1994; Schellart, 2004; Jadamec and Billen, 2010]. The addition of this less dense asthenosphere to the wedge would also enhance rollback of the slab segment [Schellart *et al.*, 2007; Soto *et al.*, 2009]. The upwelling of hot asthenospheric mantle to shallower depths also warms the mantle wedge, which may promote uplift, extension, and magmatism of the overriding plate [Bandy *et al.*, 1995; Zandt and Humphreys, 2008; Nolet, 2009; Yang *et al.*, 2009] or produce anomalous melting patterns at the slab edge (i.e., adakites) [Yogodzinski *et al.*, 2001]. The Rivera-Cocos plate boundary in the Mexican subduction zone is an example locality where such a seismic anisotropy pattern indicative of toroidal flow is spatially coincident with observed rifting (i.e., Colima Graben and El Gordo Graben) and magmatism (i.e., Colima Volcano) in the overriding North American plate along a tomographically imaged gap between the two slabs [Soto *et al.*, 2009; Yang *et al.*, 2009]. This tear between the plates was the result of the first fragmentation of the Cocos plate, when the Rivera plate separated from the proto-Cocos plate about 10 Ma [Klitgord and Mammerickx, 1982; DeMets and Traylen, 2000].

The transitions from flat to normal subduction of the Cocos plate that occur in western and eastern central Mexico are ideal locations for possible slab tear development. On the basis of structural modeling results and seismic and tectonic observations in the west, Dougherty *et al.* [2012] proposed that the Cocos slab is currently fragmenting into a North Cocos plate and a South Cocos plate along the projection of the Orozco Fracture Zone (OFZ) by a process analogous to that which occurred when the Rivera plate separated from the proto-Cocos plate [Bandy *et al.*, 2000]. In the east, observations of a sharp transition in slab dip coupled with the abrupt end of the Trans-Mexican Volcanic Belt (TMVB) suggest a second possible slab tear located within the subducted South Cocos plate. In order to test this hypothesis, we use regional earthquakes recorded by the Meso America Subduction Experiment (MASE) [MASE, 2007], Veracruz-Oaxaca (VEOX) [VEOX, 2010], Servicio Sismológico Nacional (SSN), and Oaxaca Network (OXNET) seismic arrays to study the fine-scale structure of the central Mexico subduction zone along the eastern transition from flat to normal subduction (Figure 1). We use observed waveform complexities to map the lateral extent of a thin ultra-slow velocity layer (USL) that was imaged atop the flat Cocos slab by the MASE array [Pérez-Campos *et al.*, 2008; Song *et al.*, 2009; Kim *et al.*, 2010] to test if the USL ends along a lineament related to the end of the TMVB or the sharp transition in slab dip. We also analyze seismicity patterns and focal mechanism orientations for any indications of fragmentation of the subducted plate. Additionally, we perform 1-D and 2-D waveform modeling to image the structure of the South Cocos slab and overriding plate in this region.

2. Tectonic Setting

The Cocos plate is subducting beneath the North American plate along the Middle America Trench (MAT) in central Mexico with convergence rate and plate age (11–23 Ma) increasing toward the east. This young oceanic plate exhibits large lateral variations in slab dip, with a shallow subhorizontal segment bounded by segments that dip much more steeply: $\sim 50^\circ$ near the Rivera-Cocos plate boundary and $\sim 30^\circ$ near the Isthmus of Tehuantepec [Pardo and Suárez, 1995]. Receiver functions and seismic velocity tomography along the MASE array show that the subducted Cocos plate is horizontal for about 250 km beneath the North American plate in the Guerrero region, before transitioning to a much steeper dip of 75° at the southern margin of the TMVB and truncating at a depth of 500 km [Pérez-Campos *et al.*, 2008; Husker and Davis, 2009; Kim *et al.*, 2010]. Along the transition from flat to normal subduction to the west of this region, waveform modeling and seismic anisotropy analysis suggest a tear in the Cocos slab along the landward projection of the OFZ [Dougherty *et al.*, 2012; Stubbins *et al.*, 2012]. This tear is proposed to indicate ongoing fragmentation of the Cocos slab into North Cocos and South Cocos plates, respectively [Bandy *et al.*, 2000; Dougherty *et al.*, 2012].

The along-strike variation in slab dip is evident in the $\sim 16^\circ$ oblique to the trench orientation of the TMVB, unlike volcanic arcs in most other subduction zones which are oriented trench-parallel. The TMVB is comprised of nearly 8000 volcanic structures, including large stratovolcanoes, monogenetic cones, shield volcanoes, calderas, lava flows, and domes [Macías, 2007], covering a region about 1000 km long and 80–230 km wide [Gómez-Tuena *et al.*, 2007]. Trenchward migration of the volcanic front since the late Miocene suggests ongoing rollback of the slab [Ferrari *et al.*, 2011]. In the east, the TMVB abruptly ends near

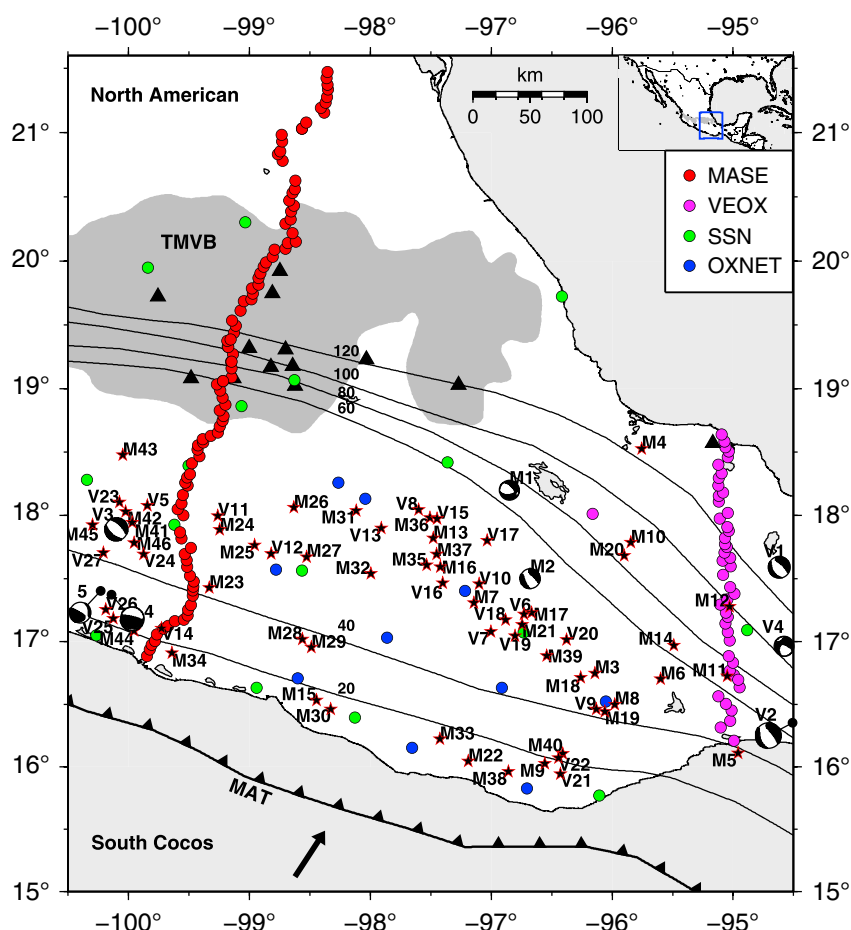


Figure 1. Map showing the locations of MASE, VEOX, SSN, and OXNET stations along with events (stars, focal mechanisms) used in this study. Event labels indicate whether the earthquake occurred during the MASE (M) or VEOX (V) array deployment. Focal mechanisms are from the Global Centroid Moment Tensor (GCMT) catalog (Table 1). The dark gray shaded area indicates the Trans-Mexican Volcanic Belt (TMVB), and the black triangles denote active volcanoes. Slab isodepth contours based on local seismicity and teleseismic receiver functions [Pérez-Campos *et al.*, 2008; Kim *et al.*, 2010, 2011; Melgar and Pérez-Campos, 2011] are shown in thin lines. The convergence direction of the South Cocos plate near the Middle America Trench (MAT) is indicated by the black arrow [DeMets *et al.*, 2010]. See Figure S1 in the supporting information for station names.

the Gulf of Mexico, accompanied by a steep topographic gradient between the high peaks of large stratovolcanoes and the coastal Veracruz Basin (Figure 2a). Post 10 Ma volcanism in the region between the eastern end of the TMVB and the Central America arc is discontinuous, including only a few isolated volcanic features, such as the Los Tuxtlas Volcanic Field (LTVF) near the Gulf of Mexico coast (Figure 2a) [Ferrari *et al.*, 2011]. LTVF volcanism began ~7 Ma, but the mechanisms of its origin are unclear [e.g., Nelson *et al.*, 1995; Ferrari *et al.*, 2005; Verma, 2006]. If the South Cocos slab is projected beneath the LTVF, it would lie at ~250 km depth, or deeper if truncated as suggested by observations of a southward dipping Yucatán slab [Kim *et al.*, 2011; Chen and Clayton, 2012]. This truncation at ~120–150 km depth constricts flow in the mantle wedge for both systems and may explain the unusual configuration of arc volcanism in the region [Kim *et al.*, 2011; Chen and Clayton, 2012].

In the oceanic domain, the South Cocos plate morphology is characterized by several tectonic structures, such as fracture zones, seamounts, and faults. Linear zones of weakness in the oceanic plate will be discussed in section 4. The O’Gorman Fracture Zone (OGFZ) intersects the MAT off the coast of Oaxaca [Singh and Mortera, 1991] and has been suggested to be the remnant of a small offset of spreading segments of the short-lived Mathematician ridge [Mammerickx and Klitgord, 1982] that is identified as a deep trough [Klitgord and Mammerickx, 1982]. Other studies of the OGFZ in the vicinity of the East Pacific Rise argue that it is not a fracture zone at all but simply a chain of seamounts that extends 50–200 km from the ridge

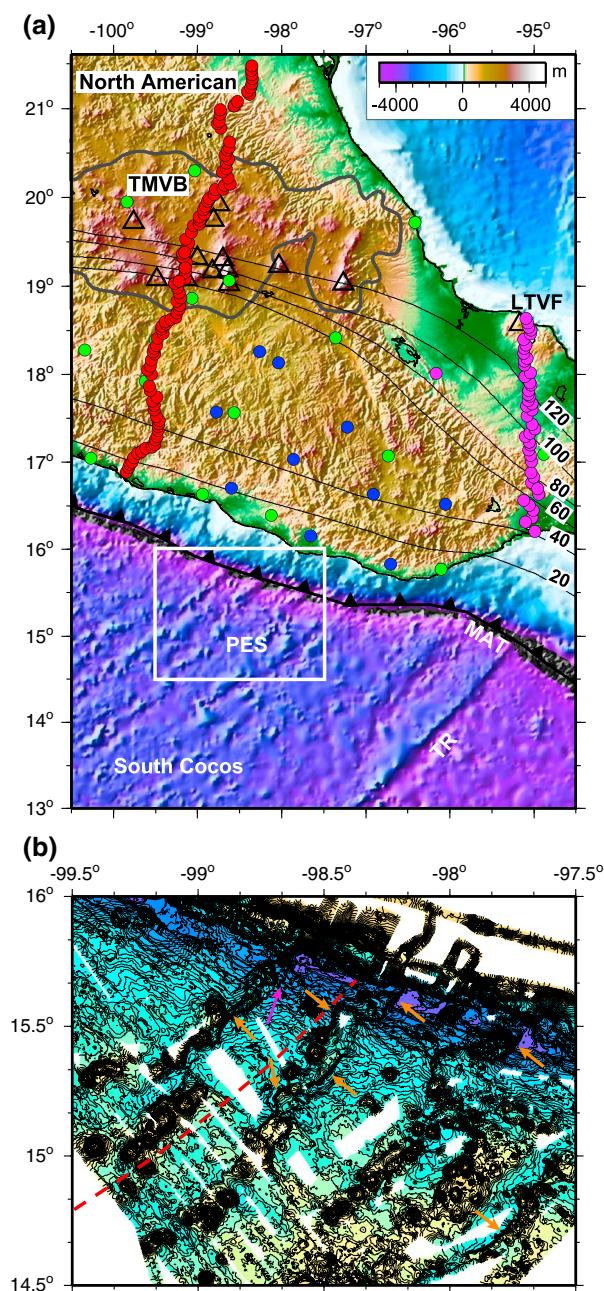


Figure 2. (a) Topographic-bathymetric map illustrating the abrupt end of the TMVB (outlined in gray) with a steep gradient in elevation and the interruption of arc volcanism. The locations of Los Tuxtlas Volcanic Field (LTVF) and the Puerto Escondido seamounts (PES) [Kanjorski, 2003] are indicated. Station locations are as in Figure 1, and open triangles denote active volcanoes. The Tehuantepec Ridge (TR) is also shown. (b) Enlarged bathymetric map of region outlined by white box in (a) showing lines of seamounts entering the MAT (dark blue region oriented NW-SE) (modified from Kanjorski [2003]). Large seamounts can be seen to enter the trench unbroken (pink arrow). Examples of seamount-parallel faulting are indicated by orange arrows. The previously identified location of the O'Gorman Fracture Zone is also shown (red dashed line).

axis [Batiza *et al.*, 1989; McClain and Wright, 1990]. This is in agreement with Kanjorski's [2003] finding that no OGFZ exists at the MAT based on the lack of significant age offsets across the proposed fracture zone. Rather, Kanjorski [2003] identified several parallel ridges composed of small to medium sized (up to ~20 km diameter and 1700 m high) seamounts created as off-axis volcanism entering the MAT in this region, with the larger seamounts remaining physically intact throughout the subduction process (Figure 2b). Included in this zone is the Puerto Escondido seamount cluster, a broad volcanic feature littered with >100 volcanic cones and accompanying lava flows (Figure 2) [Kanjorski, 2003]. Observed seamount-parallel normal faulting (Figure 2b) is shown to be seismically active [Kanjorski, 2003].

3. Data Analysis

3.1. Data

The seismic data used in this study were recorded by the MASE, VEOX, SSN, and OXNET arrays. The MASE array consisted of 100 broadband seismic instruments deployed from January 2005 to June 2007 in a trench-perpendicular line in the Guerrero region with a station spacing of ~5 km (Figure 1). Across the Isthmus of Tehuantepec, the 45 broadband seismometers of the VEOX array were deployed in a 300 km long line from August 2007 to March 2009 (Figure 1). The goal of these experiments was to image the structure of the Mexican subduction zone in the flat slab and normal dipping regions, respectively. The permanent SSN array consists of 37 broadband seismic instruments located throughout Mexico, of which, 16 are utilized in this study (Figure 1). In the Oaxaca region, located between the MASE and VEOX arrays, 10 broadband seismometers were installed in a 2-D geometry in 2006 as part of the OXNET array (Figure 1) in an effort to detect and monitor nonvolcanic tremor and microseismicity signals in this region [Brudzinski *et al.*, 2010]. A map of the station names for all four arrays is shown in Figure S1 in the supporting information.

We analyze seismograms from 75 regional intraslab earthquakes recorded by these arrays. These events have magnitudes

Table 1. Events Used in This Study and Their Source Parameters

Event ID	Date	Latitude (deg)	Longitude (deg)	Depth (km)	Magnitude (M_w)	Mechanism Strike/Dip/Rake	Source ^a
4	2007/04/13	17.37	−100.14	39	5.99	279/42/86	1 ^b
				43	6.0	284/73/92	2
				41	5.9	303/79/98	3
				20	5.7	267/61/85	4
5	2007/04/13	17.40	−100.23	30	5.30	70/41/2	1 ^b
				67	5.3	28/29/0	2
				36	5.3	39/17/6	3
				35	5.3	117/84/−101	4
M1	2005/09/24	18.20	−96.85	68	5.17	316/64/−66	1 ^b
				61	5.0	320/56/−46	2
				104	5.1	329/57/−42	3
M2	2007/05/04	17.50	−96.68	59	5.08	139/32/−75	1 ^b
				60	5.0	176/46/−46	2
				70	5.0	192/51/−40	3
M3	2007/02/14	16.749	−96.142	67	4.71	9/70/−58	1 ^c
				81	4.7	327/66/−65	3
M4	2005/11/14	18.528	−95.757	64	4.81	335/50/−60	1 ^c
				28	4.4	320/34/−77	3
M5	2006/01/26	16.111	−94.957	82	4.73	255/71/−62	1 ^c
M6	2007/06/02	16.701	−95.600	80	4.74	9/47/46	1 ^c
M7	2005/09/08	17.306	−97.145	70	4.82	345/35/4	1 ^c
M8	2005/09/29	16.500	−95.980	67	4.36	246/61/−49	1 ^c
				76	4.2	174/24/10	3
M9	2006/11/08	16.027	−96.558	43	5.23	348/36/−44	1 ^c
				38	5.1	352/35/−44	2
				45	4.9	288/85/98	3
M10	2006/03/17	17.786	−95.844	124	4.52	204/16/−43	1 ^c
M11	2005/12/17	16.725	−95.048	99	4.73	180/71/−84	1 ^c
M12	2007/03/01	17.279	−95.029	142	4.70	45/67/−20	1 ^c
M13	2005/09/07	17.820	−97.480	72	4.20	149/50/−64	1 ^c
M14	2006/02/22	16.969	−95.489	123	4.53	121/64/−1	1 ^c
M15	2005/06/06	16.534	−98.444	59	4.42	281/45/−40	1 ^c
M16	2006/09/18	17.593	−97.422	69	4.35	140/31/51	1 ^c
M17	2006/06/08	17.228	−96.666	86	4.45	328/78/−26	1 ^c
M18	2005/12/22	16.713	−96.259	84	4.50	350/43/−81	1 ^c
M19	2006/12/21	16.443	−96.060	77	5.25	36/19/−5	1 ^c
M20	2006/02/09	17.684	−95.901	104	4.62	226/56/−86	1 ^c
M21	2006/01/19	17.134	−96.743	55	4.60	146/81/5	1 ^c
M22	2005/11/01	16.044	−97.192	54	4.28	70/59/−60	1 ^c
M23	2005/05/20	17.428	−99.330	38	4.39	195/48/74	1 ^c
M24	2006/09/01	17.888	−99.244	61	4.54	74/64/−44	1 ^c
M25	2006/09/22	17.763	−98.958	45	4.43	298/47/21	1 ^c
M26	2006/09/07	18.064	−98.633	56	4.15	113/65/36	1 ^c
M27	2006/11/12	17.673	−98.528	64	4.44	331/70/−72	1 ^c
M28	2005/10/03	17.020	−98.561	35	4.05	350/69/−41	1 ^c
M29	2006/11/30	16.954	−98.488	56	4.28	198/84/47	1 ^c
M30	2005/06/06	16.461	−98.327	54	4.34	279/81/6	1 ^c
M31	2006/06/09	18.038	−98.117	57	4.23	290/87/53	1 ^c
M32	2006/07/24	17.539	−97.995	70	4.27	132/67/−20	1 ^c
M33	2006/11/28	16.223	−97.426	59	4.06	241/51/−75	1 ^c
M34	2007/01/02	16.910	−99.640	45	4.62	345/75/69	1 ^c
M35	2005/02/11	17.607	−97.534	54	4.38	36/43/−22	1 ^c
M36	2007/02/09	17.981	−97.505	79	3.90	70/50/−60	1 ^c
M37	2007/06/05	17.694	−97.453	70	4.26	10/44/−31	1 ^c
M38	2006/03/12	15.962	−96.859	54	4.35	83/61/−57	1 ^c
M39	2006/03/22	16.886	−96.541	63	4.38	350/54/−87	1 ^c
M40	2006/11/08	16.106	−96.409	52	4.30	99/44/60	1 ^c
M41	2005/05/26	17.946	−99.970	53	5.00	13/61/−60	1 ^c
				62	4.8	296/41/−80	3
				50	4.6	289/34/−76	4
M42	2006/06/26	18.032	−100.023	51	4.65	345/58/−28	1 ^c
				50	4.3	293/35/−79	4
M43	2007/05/28	18.478	−100.046	52	4.45	217/76/−83	1 ^c

Table 1. (continued)

Event		Latitude	Longitude	Depth	Magnitude	Mechanism	
ID	Date	(deg)	(deg)	(km)	(M_w)	Strike/Dip/Rake	Source ^a
M44	2007/06/18	17.086	−99.953	42	4.21	57/40/18	1 ^c
M45	2005/11/21	17.925	−100.295	56	4.19	26/76/26	1 ^c
M46	2005/04/30	17.784	−99.952	77	4.45	16/61/−40	1 ^c
V1	2007/09/15	17.59	−94.62	149	5.44	308/65/−85	1 ^b
				144	5.4	309/61/−108	2
V2	2008/02/12	16.35	−94.51	86	6.52	155/42/−81	1 ^b
				87	6.5	178/35/−54	2
V3	2008/04/28	17.89	−100.10	64	5.80	175/54/−51	1 ^b
				56	5.8	129/42/−96	2
				52	5.8	131/46/−97	3
				50	5.4	138/40/−88	4
V4	2009/02/18	16.96	−94.58	117	4.99	174/41/−55	1 ^b
				121	4.9	193/54/−22	2
V5	2007/10/12	18.078	−99.845	52	4.13	256/68/−3	1 ^c
V6	2007/12/13	17.218	−96.728	80	4.57	210/74/−58	1 ^c
V7	2008/12/15	17.078	−97.004	69	4.38	209/54/−46	1 ^c
				65	4.4	154/43/−82	3
V8	2009/01/27	18.047	−97.602	66	4.28	20/40/−49	1 ^c
V9	2007/11/04	16.460	−96.131	75	4.47	56/61/25	1 ^c
V10	2007/11/12	17.457	−97.102	66	4.37	209/63/−29	1 ^c
V11	2008/08/21	17.996	−99.263	50	4.31	8/22/−49	1 ^c
V12	2008/03/08	17.699	−98.819	42	4.46	298/75/69	1 ^c
V13	2008/04/05	17.899	−97.909	61	4.17	341/67/39	1 ^c
				54	4.0	310/46/−78	3
V14	2007/08/18	17.106	−99.725	78	4.48	110/60/−16	1 ^c
V15	2008/07/18	17.976	−97.447	57	4.21	7/36/−25	1 ^c
V16	2008/12/11	17.466	−97.402	56	4.15	196/40/−61	1 ^c
V17	2008/03/18	17.802	−97.032	90	4.49	195/86/−73	1 ^c
V18	2007/11/28	17.174	−96.881	83	3.96	190/65/−70	1 ^c
V19	2008/06/01	17.046	−96.805	50	3.80	134/61/−79	1 ^c
V20	2008/01/09	17.016	−96.377	79	4.25	11/84/19	1 ^c
V21	2009/02/02	15.944	−96.429	47	4.13	180/41/7	1 ^c
V22	2008/06/20	16.071	−96.442	49	4.10	230/55/−85	1 ^c
V23	2009/01/14	18.104	−100.073	46	4.40	120/41/−80	1 ^c
				46	4.3	129/49/−100	3
V24	2008/05/18	17.694	−99.874	73	4.36	191/70/−25	1 ^c
V25	2008/10/08	17.184	−100.126	47	4.26	188/81/19	1 ^c
V26	2009/02/01	17.253	−100.189	36	3.91	312/76/59	1 ^c
V27	2008/02/23	17.703	−100.208	63	4.38	175/85/−56	1 ^c

^aSources are (1) focal mechanism, M_w , and depth from this study; (2) focal mechanism, M_w , and depth from the Global CMT (GCMT) catalog [Dziewonski et al., 1981; Ekström et al., 2012]; (3) focal mechanism, M_w , and depth from the Servicio Sismológico Nacional (SSN) catalog; (4) focal mechanism, M_w , and depth from Pacheco and Singh [2010].

^bLocation from GCMT catalog.

^cLocation from SSN catalog.

within the range of 3.8 to 6.5 and occur at depths between 30 km and 149 km (Table 1). The locations of these events are shown in Figure 1. Earthquakes that occurred during the MASE deployment have identifiers that begin with “M,” while those that occurred during the VEOX deployment begin with “V” (Figure 1 and Table 1). Events 4 and 5 were also part of the Dougherty et al. [2012] dataset, so their identifiers have been maintained for clarity. Note that both of these events occurred during the MASE deployment (Table 1).

3.2. Slab Dip

The lateral variation in slab dip across the transition from flat to normal subduction in eastern central Mexico is examined in detail to assess if this change in geometry is accommodated by a smooth contortion of the slab, or if there is an abrupt transition which could be indicative of a possible tear. Epicenters for earthquakes from the January 2001 to May 2011 event catalog of the SSN are mapped and divided into twenty-one 25 km wide trench-normal bins (Figure 3a). The locations of events furnished by the SSN have been carefully revised by an analyst, and the accuracy of the catalog is confirmed by a relocation study [Alberto, 2010]. Bin 1 overlies the flat slab region located along the MASE array and bin 21 overlies the normal dipping region

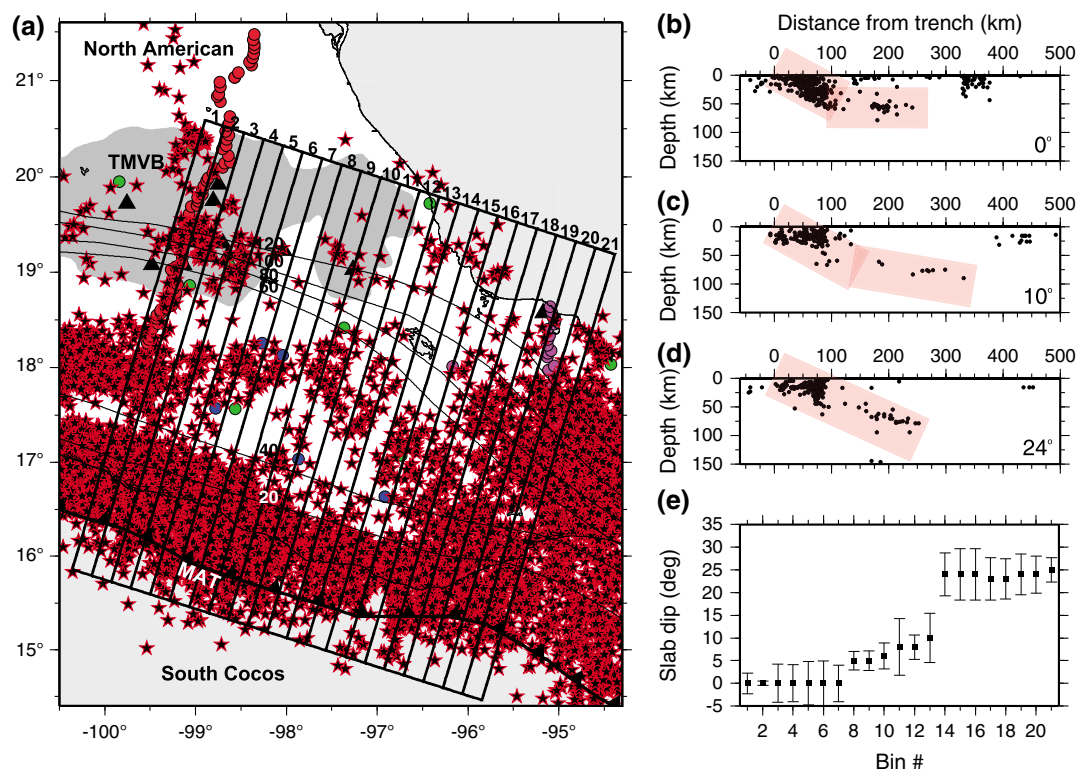


Figure 3. Seismicity and slab dip across the transition from flat to normal subduction located to the east of the MASE array. (a) Map showing epicenters (stars) for earthquakes from the January 2001 to May 2011 SSN event catalog. Data in twenty-one 25 km wide bins roughly perpendicular to the MAT are analyzed for changes in slab dip across this region. Cross sections of seismicity in bins (b) 2, (c) 13, and (d) 14 are shown along with their respective estimated slab dips. Note the significant change in slab dip between bins 13 and 14. (e) Plot of slab dip across the data bins. Error bars are weighted by the number of events in each bin, such that fewer events produce a larger error.

across the VEOX array (Figure 3a). Cross sections of the seismicity in each bin illustrate variations in the Wadati-Benioff zone across the region and are used to estimate the slab dip in each bin. Examples from bins 2, 13, and 14 are shown in Figures 3b–3d. The dip angle is estimated by visually selecting hypocenter locations that are downdip of the trench and not within the overriding plate (as defined by teleseismic receiver functions [Pérez-Campos *et al.*, 2008; Kim *et al.*, 2010, 2011; Melgar and Pérez-Campos, 2011]), then performing a linear regression of the selected locations. The estimated slab dip in each of the 21 bins is shown in Figure 3e. The errors on these dip estimates (calculated from the standard deviation in dip) are weighted by the number of earthquakes in each bin, such that fewer events in a bin produce a larger error, with values ranging from $\pm 0.49^\circ$ (bin 2) to $\pm 6.3^\circ$ (bin 11). The slab is flat beneath the MASE array with its dip gradually increasing across the easternmost TMVB region to 10° by bin 13 (Figure 3). Between bins 13 and 14, there is a sharp 14° increase in slab dip, followed by an approximately constant dip (23 – 25°) across the remainder of the bins to the east (Figure 3).

3.3. Ultra-Slow Velocity Layer

The USL that was imaged atop the flat Cocos slab beneath the MASE array is a 3–5 km thick layer with a V_p of 5.4–6.2 km/s and a V_s of 2.0–3.4 km/s [Song *et al.*, 2009; Kim *et al.*, 2010]. The exact nature of the USL is not known, but its anomalously low shear wave velocity suggests a relationship with fluids, specifically free water or hydrous minerals, in the subduction zone. Song *et al.* [2009] proposed that the USL represents a fluid-saturated portion of the oceanic crust, forming a high pore fluid pressure (HPFP) layer that is sealed by some low permeability layer, such as fine-grained blueschist, directly above it. In their thermal modeling of the central Mexico subduction zone, Manea *et al.* [2004] found a high pore pressure ratio of 0.98 along the subduction interface, consistent with Song *et al.*'s [2009] HPFP layer. Kim *et al.* [2010], on the other hand, proposed that the USL is upper oceanic crust that is highly heterogeneous and composed of mechanically weak hydrous minerals (talc) that might be under high pore pressure. With or without free fluid, Kim *et al.* [2013] demonstrate that a talc-rich ultramafic layer is required to explain the observed USL velocities and suggest

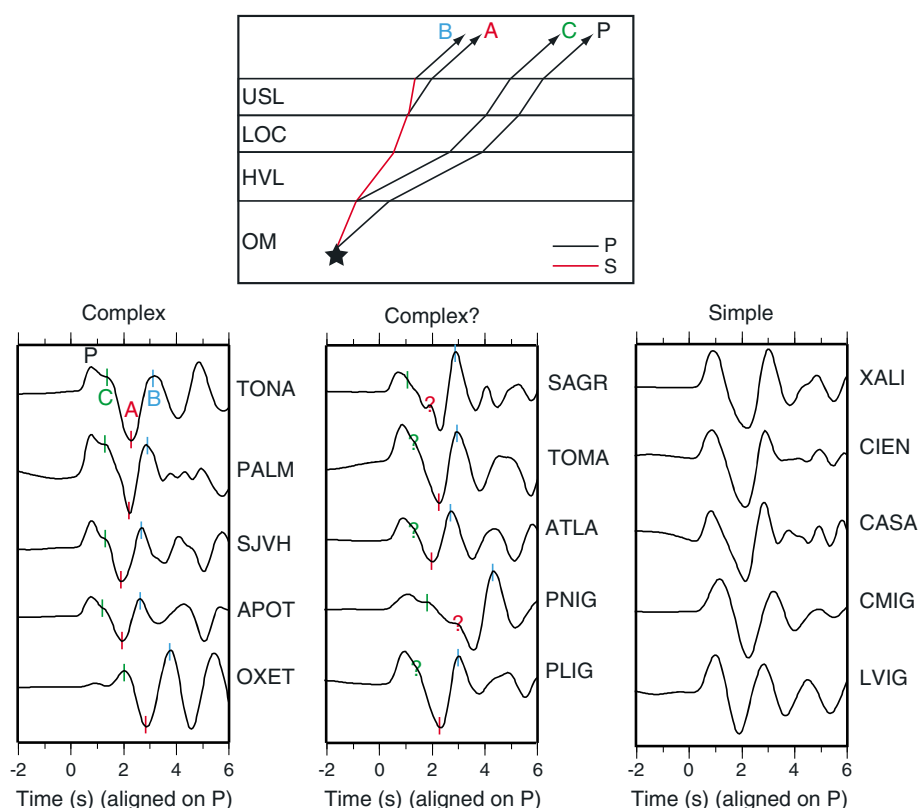


Figure 4. (top) Schematic illustrating the raypaths of the P wave and the three S -to- P phases (A, B, C) that comprise the complex P waveform. Abbreviations are USL, ultra-slow velocity layer; LOC, lower oceanic crust; HVL, high velocity layer; OM, oceanic mantle. (bottom) Examples of (left) complex, (middle) possibly complex, and (right) simple P waveforms from event M2 recorded on the vertical component by MASE, SSN, and OXNET stations and filtered to 0.01–0.6 Hz. S -to- P phases A, B, and C are indicated by red, blue, and green tick marks, respectively. All three of these phases are visible in the complex waveforms within 4 s of the P wave. Question marks on the possibly complex waveforms indicate a phase that is not easily identified due to an uncharacteristic pulse shape and/or amplitude. Simple waveforms lack the shoulder in the direct P pulse indicative of the C phase and also have uncharacteristically shaped and/or low amplitude A and B phases, indicating there is no USL present. Modified from Dougherty *et al.* [2012].

that this talc originates from the mantle wedge during the slab flattening process. Similarly, Manea *et al.* [2013] propose that the USL represents a remnant of mantle wedge that experienced significant serpentinization since the slab flattened. The hydrous minerals and/or high pore pressure of the USL can explain the observed decoupling of the flat slab from the overriding plate, as evidenced by the lack of compressional seismicity in the North American plate [Singh and Pardo, 1993] and GPS observations [Franco *et al.*, 2005], and may be responsible for the flat subduction geometry, shown to be facilitated and sustained by such a low-strength layer [Manea and Gurnis, 2007; Kim *et al.*, 2010].

The presence of the USL atop the South Cocos slab is identified by the existence of complex P waveforms [Song *et al.*, 2009] recorded by the MASE or VEOX, SSN, and OXNET arrays. As described by Dougherty *et al.* [2012], these complex P waveforms consist of three locally converted S -to- P phases (A, B, C) that arrive within 4 s after the P wave (Figure 4). Phase A converts at the bottom of the USL and appears as a negative pulse at local stations. Phase B arrives immediately after phase A as a positive pulse, indicative of an S -to- P wave that converted at the top of the USL. Phase C converts at the base of the high-velocity layer, arriving before phase A and ~ 1.0 – 1.5 s after the direct P wave. These three phases are searched for in the seismograms of the intraslab earthquakes analyzed in this study. P waveforms in these seismograms are categorized as complex, possibly complex, or simple based on the existence and nature of phases A, B, and C. Examples of these waveforms from event M2 recorded at MASE, SSN, and OXNET stations are shown in Figure 4. The waveforms have been bandpass filtered to 0.01–0.6 Hz, with the shorter periods in the frequency band allowing for the identification of the three S -to- P phases. When all three of the phases are readily observed, the waveform is deemed complex. If one of the phases is not easily identified due to an

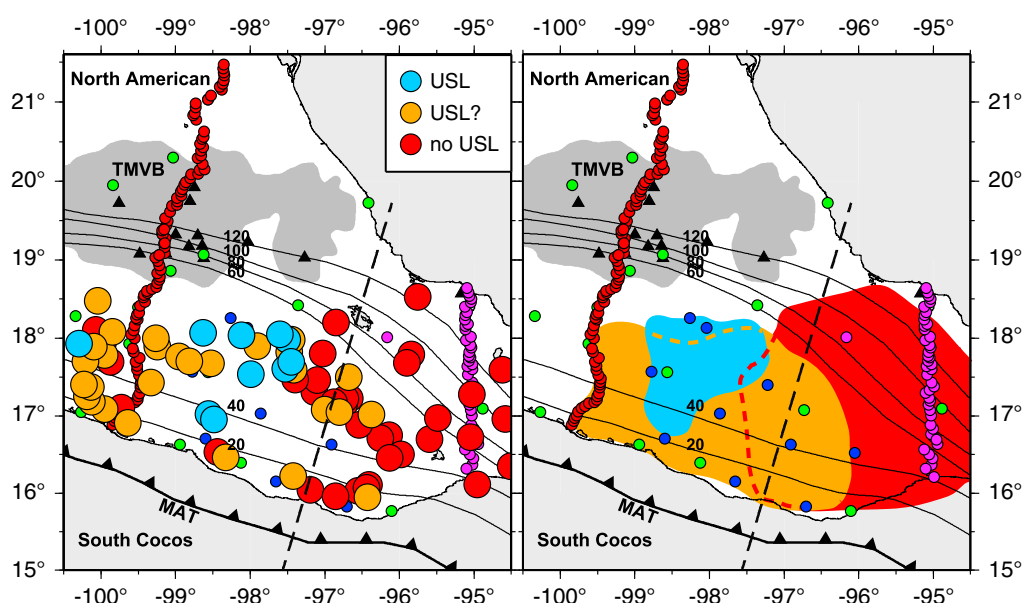


Figure 5. Mapping the eastern lateral extent of the USL using MASE, VEOX, SSN, and OXNET *P* waveforms. (left) Events which indicate the presence of the USL are shown in cyan. Those which possibly indicate the USL is present are shown in orange. Red events indicate no USL is present. See Figure S2 in the supporting information for enlarged map including event labels. (right) Shaded contours of USL, possible USL, and no USL zones. The boundary between bins 13 and 14 of Figure 3, demarking the significant change in slab dip, is denoted by the black dashed line.

uncharacteristic pulse shape and/or amplitude, but the other two phases are clearly visible, then the waveform is possibly complex. Simple waveforms lack the shoulder in the direct *P* pulse representative of the C phase and also have uncharacteristically shaped and/or low amplitude A and B phases, indicating that there is no USL present.

The eastern lateral extent of the USL is mapped by examining the status of the layer at each epicentral event location (Figure 5). We identify 10 events which indicate the presence of the USL from their *P* waveforms. Another 28 events possibly indicate the presence of the USL. The remaining 37 events in our dataset indicate no USL is present at their locations. An enlarged USL status map that includes event labels can be found in Figure S2. In general, the events which suggest (or possibly suggest) the occurrence of the USL are concentrated in the western portion of the study region, south of the TMVB, while those that suggest the USL is lacking are concentrated in the east, where the slab dip increases. A handful of possible USL locations overlap the predominantly no USL region near the location of the sharp transition in slab dip, marked by the boundary between bins 13 and 14 of Figure 3a (Figure 5). Concentrating on the area east of the MASE array, we draw shaded contours of the USL, possible USL, and no USL zones for clarity of observation (Figure 5). Note that the boundary between the USL and no USL zones is approximately coincident with the eastern end of the TMVB along a trench-normal transect.

3.4. Seismicity

Intraslab seismicity across the study region is analyzed for any changes, gaps, or patterns that could elucidate the nature of the transition from flat to normal subduction of the South Cocos plate. Epicentral locations of 40–80 km depth earthquakes from the 1960 to 2012 International Seismological Centre (ISC) Bulletin event catalog [International Seismological Centre, 2011] are mapped and divided into the same twenty-one 25 km wide bins used to estimate the lateral variation in slab dip (Figure 6). Examination of the number of earthquakes in each bin, in conjunction with the event map, reveals a ~75 km wide zone of decreased intraslab seismicity (bins 11–13), which is indicative of a structural change, located immediately west of the sharp transition in slab dip. The western limit of this decreased seismicity zone encompasses the easternmost tip of the TMVB. While the three bins that comprise this zone each contain a low number of earthquakes, the spatial distribution of the seismicity in bins 12 and 13 is noticeably sparser than that in bin 11 (Figure 6). In particular, downdip seismicity in bins 12 and 13 is concentrated near 97.25°W, 17.25°N, extending linearly to the northeast, with gaps in the seismicity observed along either side. Additionally,

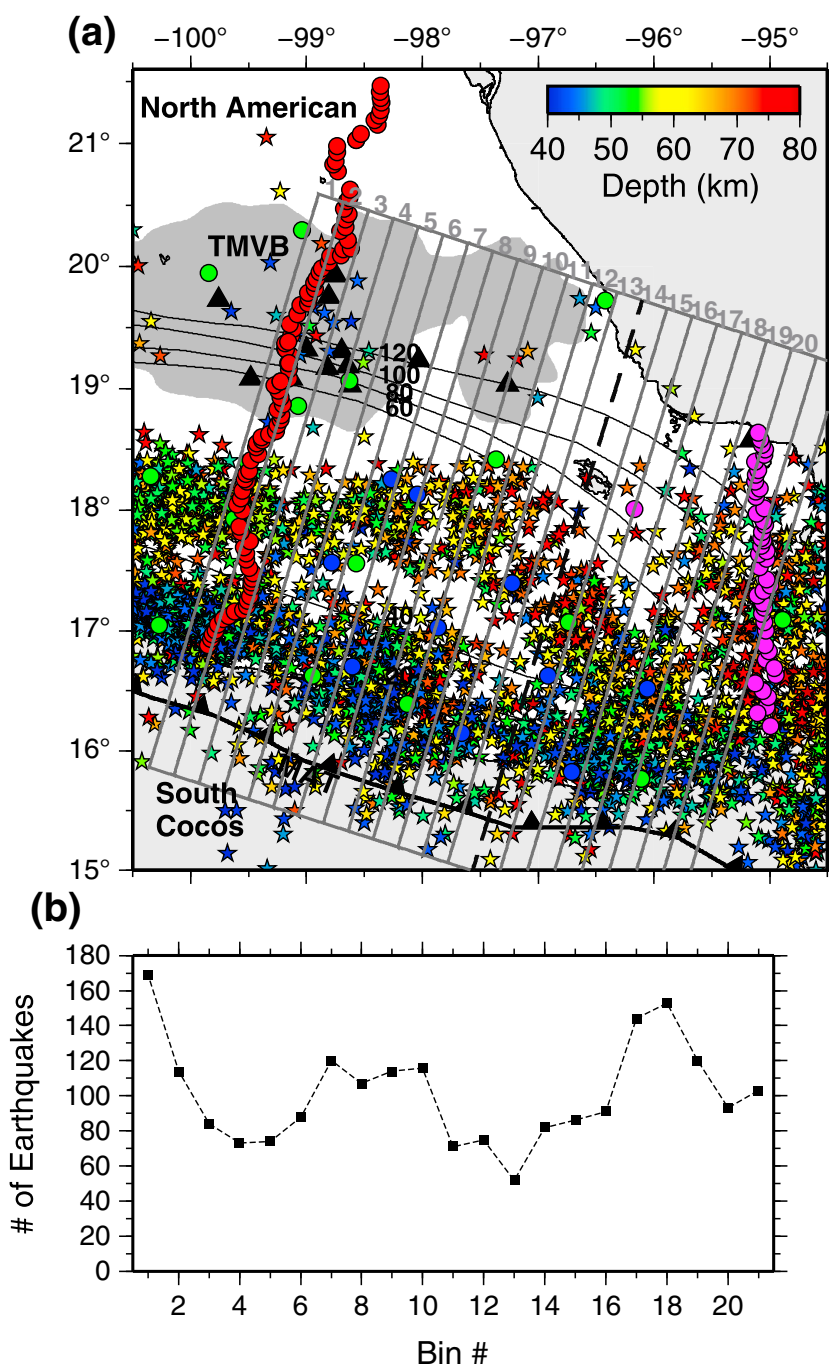


Figure 6. Intraslab seismicity across the study region. (a) Map of epicenters (stars) for 40–80 km depth earthquakes from the 1960–2012 International Seismological Centre (ISC) Bulletin event catalog [International Seismological Centre, 2011]. Epicenters are color-coded by event depth. Data in the same 25 km wide bins as Figure 3 are analyzed for changes in intraslab seismicity across this region. (b) Plot of number of earthquakes per bin for the 21 bins analyzed. Note the ~75 km wide zone of decreased seismicity immediately west of the sharp transition in slab dip (black dashed line), encompassing bins 11–13.

seismicity updip is concentrated in a small area between the coast and the 20 km isodepth contour. This scattered distribution suggests that the events in these bins may be occurring in clusters.

The broadscale distribution of intraslab seismicity west of the VEOX array can be described by two overall trends: (1) a WNW-ESE oriented band along the coast and (2) an E-W oriented downdip zone that rotates to a NW-SE orientation at the eastern end of the TMVB (Figure 6a). The downdip zone is spatially offset from

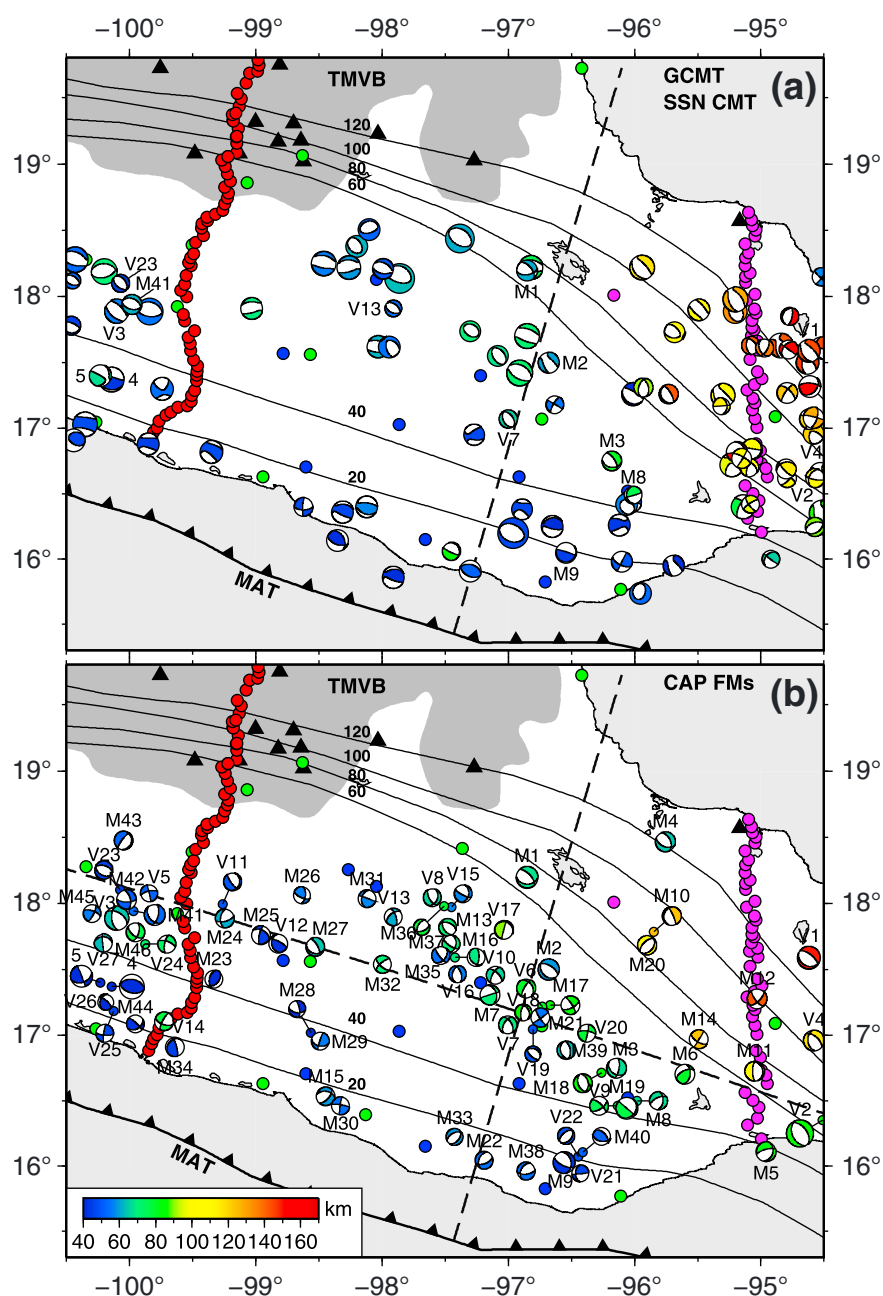


Figure 7. Focal mechanism maps for intraslab earthquakes which occurred in the study region. (a) Map of focal mechanisms from the January 1976 to November 2012 Global CMT (GCMT) catalog [Dziewonski *et al.*, 1981; Ekström *et al.*, 2012] and the January 2000 to November 2012 SSN CMT catalog. Events analyzed in this study are labeled for comparison. (b) Map of focal mechanisms inverted for using the Cut and Paste (CAP) technique in this study for the 75 earthquakes of interest. Source parameters can be found in Table 1. The black dashed lines mark the locations of trench-perpendicular (at the sharp transition in slab dip) and trench-parallel cross sections. Mechanisms are color-coded by event depth.

the coastal band by a seismicity gap that increases in width from west to east. At the point of rotation in the downdip zone orientation, a general increase in the depth of the intraslab seismicity can be observed. Coincidentally, the coastal band exhibits decreased seismicity.

Focal mechanisms of intraslab earthquakes in eastern central Mexico are also examined for details of the South Cocos slab structure. Source mechanisms of 40–170 km depth events from the January 1976 to November 2012 Global Centroid Moment Tensor (GCMT) catalog [Dziewonski *et al.*, 1981; Ekström *et al.*, 2012] and the January 2000 to November 2012 SSN CMT catalog are mapped in Figure 7a. For events which

can be found in both catalogs, only the GCMT solution is shown. West of the VEOX array, in the flat slab and transitional dip regions, there is a predominance of normal faulting events north of the 40 km isodepth contour, although the overall seismicity is scarce. This preponderance of normal faulting events is consistent with the observed decoupling of the slab from the overriding plate [Singh and Pardo, 1993; Franco *et al.*, 2005] due to the low-strength USL. It is also consistent with the typical faulting type (i.e., normal) of earthquakes which occur in the oceanic lithosphere due to bending of the slab and/or slab pull [e.g., Isacks and Barazangi, 1977; Manea *et al.*, 2006]. Across the sharp transition in slab dip, a group of events can be seen to abruptly decrease in depth from west (shallowly dipping slab) to east (more steeply dipping slab), contrary to what would be expected for this change in geometry. The deeper events in the west are coincident with the location of increased intraslab seismicity depth noted above for the ISC catalog data. The focal planes across this zone are oriented roughly normal or oblique to the change in dip line.

In addition to the GCMT and SSN CMT catalog data, we perform source mechanism inversions for the 75 earthquakes of interest in this study using the Cut and Paste (CAP) source estimation technique. This waveform modeling method, detailed in Zhao and Helmberger [1994] and Zhu and Helmberger [1996], divides broadband seismograms into body wave and surface wave segments and inverts them independently in an effort to maximize the benefits and minimize the limitations of using long- and short-period portions of broadband records. The source mechanism is obtained by applying a direct grid search of strike, dip, rake, magnitude, and depth through all possible solutions to find the global minimum of misfit between the observations and synthetics, allowing time shifts between portions of seismograms and synthetics [Zhu and Helmberger, 1996]. One of the advantages of this technique is that it proves insensitive to velocity models and lateral crustal variation, making it possible to generate accurate source mechanisms with less than perfect Green's functions [Zhao and Helmberger, 1994; Zhu and Helmberger, 1996; D'Amico *et al.*, 2010, 2011]. The focal mechanisms obtained using CAP are shown in Figure 7b and detailed in Table 1. As with the GCMT and SSN CMT catalog data, the CAP focal mechanisms show a general predominance of normal faulting events in the flat slab and transitional dip regions, although a few thrust and several strike-slip faulting events can also be seen. The patch of deeper events west of the sharp transition in slab dip also recurs in our data; however, the eastward shallowing is not as abrupt. Contrary to the catalog data, a few of the CAP source mechanisms located near the sharp transition in slab dip show focal planes orientated roughly parallel to the change in dip line, which may have important implications for the morphology of the South Cocos slab in this region.

Cross sections of the CAP focal mechanisms along trench-normal (i.e., change in dip line) and trench-parallel transects that sample the transition from flat to normal subduction are analyzed for additional details of the slab morphology (Figure 8). Hypocenters located within 50 km of each respective transect are projected on vertical planes with focal mechanisms shown as viewed from the side. For clarity, mechanisms are distinguished by faulting type following the classification of Zoback [1992], which is based on the plunge of P , T , and B axes. The faulting types include normal faulting (NF), predominantly normal faulting with a component of strike-slip (NS), strike-slip faulting (SS), predominantly thrust faulting with a component of strike-slip (TS), thrust faulting (TF), and unknown (U). The unknown faulting type describes events which do not clearly fit into any of other categories and generally applies to smaller and/or less well-constrained focal mechanisms [Zoback, 1992]. The trench-normal and trench-perpendicular cross sections further demonstrate the predominance of normal (NF and NS) mechanisms in this region that was noted above. Near the point of intersection of these two cross sections, a slight vertical spread in the distribution of events can be observed, which may be related to the nature of the sharp transition in slab dip located here. From the trench-parallel profile (Figure 8b), a concentration of strike-slip mechanisms can also be observed near the abrupt dip change, which may have further implications for the nature of this zone.

3.5. 1-D Velocity Modeling

The shallow seismic structure of the eastern central Mexico subduction zone is examined in 1-D using frequency-wave number forward modeling techniques with CAP focal mechanisms (Table 1). The sensitivity of observed waveforms to the subduction zone structure is tested using 15 different P and S wave velocity models, five of which are presented here: (1) Furumura and Singh [2002] velocity model for central Mexico without the slab (FSa) (Figure 9a), (2) Furumura and Singh [2002] velocity model including the slab (FSb) (Figure 9b), (3) new central Mexico (ncM) velocity model from Dougherty *et al.* [2012], (4) composite velocity model comprised of the overriding plate structure from model FSa and the slab structure from model ncM (ncM_FSa), and (5) modified ncM velocity model with recalculated P wave velocities (ncMc) from this

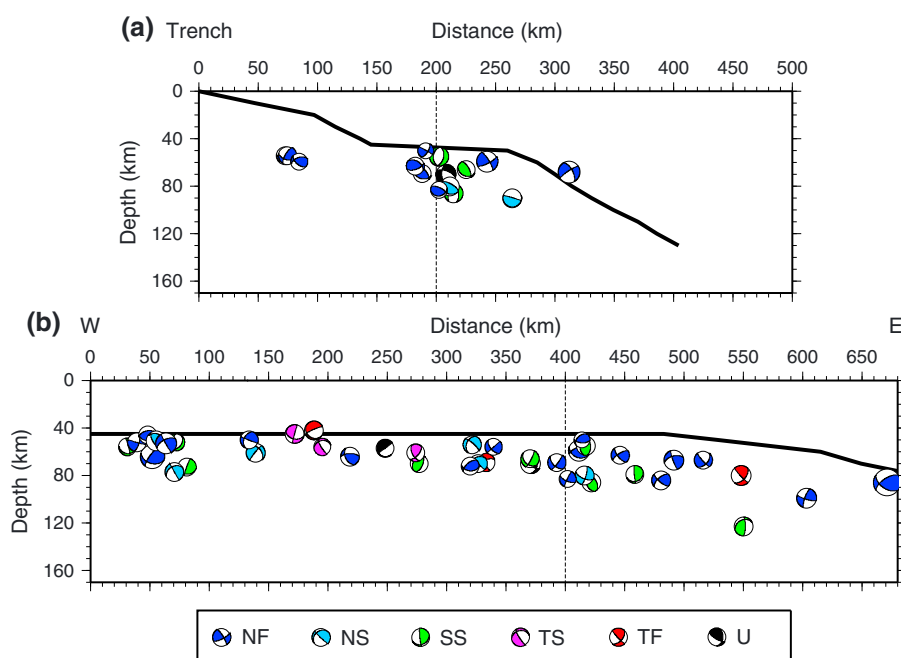


Figure 8. Cross sections of CAP focal mechanisms along the (a) trench-normal and (b) trench-parallel lines in Figure 7. Focal mechanisms located within 50 km of the respective cross-section line are included and shown as viewed from the side. Mechanisms are colored by faulting type following *Zoback [1992]*. The faulting types include normal faulting (NF), predominately normal with strike-slip component (NS), strike-slip faulting (SS), predominately thrust with strike-slip component (TS), thrust faulting (TF), and unknown (U). The majority of events shown exhibit normal (NF or NS) mechanisms. Heavy black lines indicate the top of the slab from the isodepth contours. Thin dashed lines mark the point of intersection of the two cross-sections.

study (Figure 9e). These five models are the most relevant of those tested as they provide the closest approximations of the observed waveforms. The remaining 10 models can be found in Figure S3. The FSa model does not include slab structure, while the other four models discussed here contain a multilayered, somewhat complex slab (Figure 9). The ncM, ncM_FSa, and ncMc models also include the USL (3 km thick, V_s of 2.6 km/s) that was imaged by the MASE array. The P wave velocities in the ncMc model are calculated using the FSa V_p/V_s ratio of 1.7 and ncM S wave velocities, with the thicknesses and depths of the layers held constant between the ncM and ncMc models (Figure 9e). The FSa crustal model tests the sensitivity of

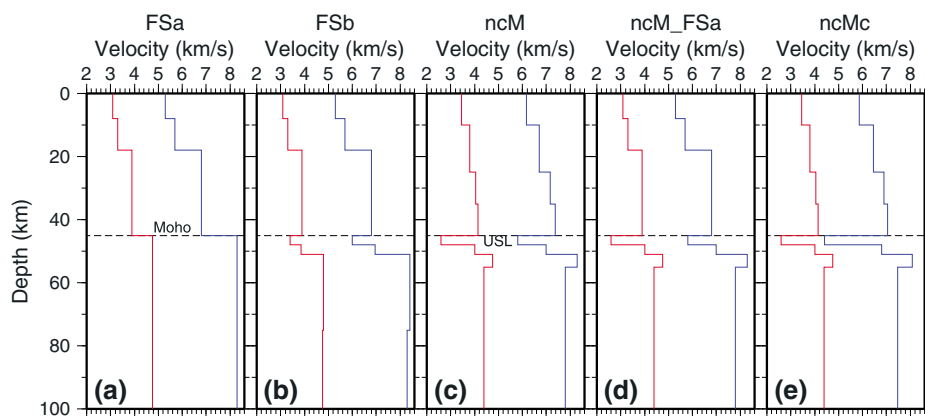


Figure 9. 1-D P (blue) and S (red) wave velocity models tested in this study. (a) *Furumura and Singh [2002]* velocity model for central Mexico without the slab (FSa). The Moho depth is indicated by the black dashed line. (b) *Furumura and Singh [2002]* velocity model including the slab (FSb). (c) New central Mexico (ncM) velocity model from *Dougherty et al. [2012]*. Ultra-slow velocity layer (USL) is indicated at the top of the subducted plate. (d) Composite velocity model comprised of the overriding plate structure from model FSa and the slab structure from model ncM (ncM_FSa). (e) Modified ncM velocity model with recalculated P wave velocities (ncMc) from this study.

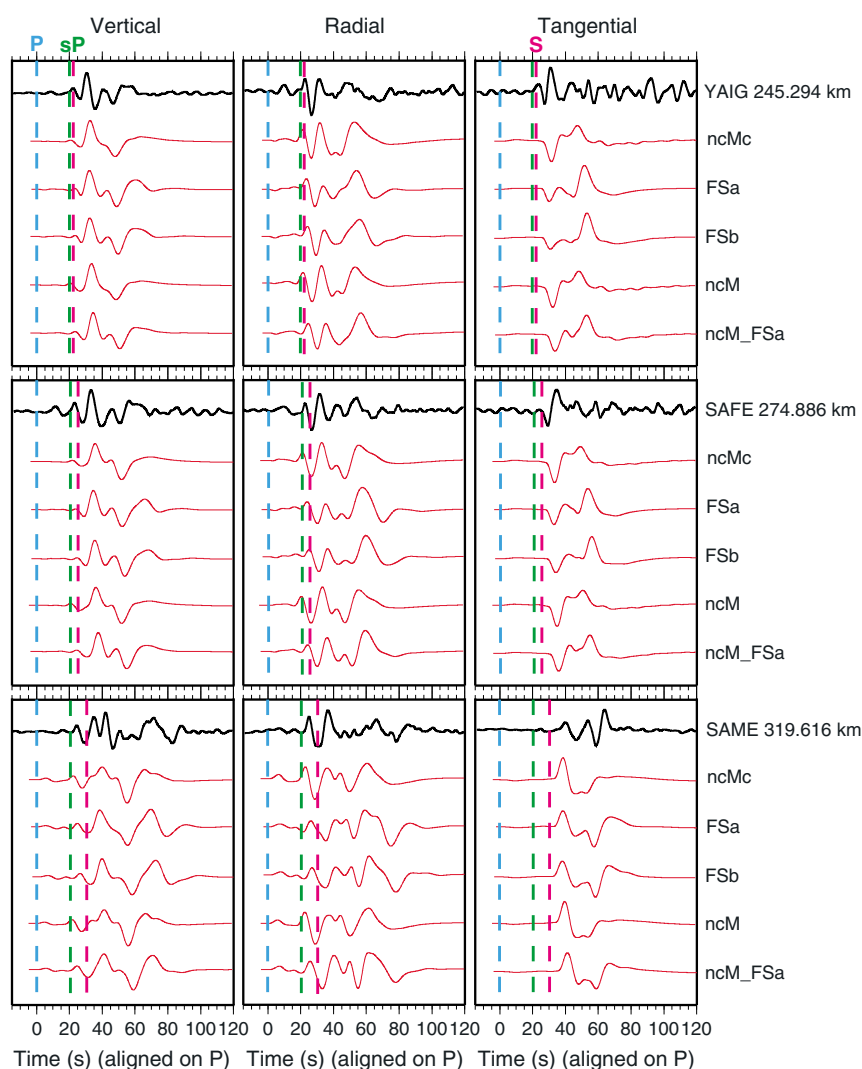


Figure 10. Comparison of 1-D modeling results of event M1 for the five models tested at three stations. Waveforms are filtered to 0.01–0.1 Hz. Data are in black, synthetics are in red. *P*, *sP*, and *S* phases are indicated by dashed lines.

the observed waveforms to the crustal structure only, while the remaining four models test the waveform sensitivity to combined crustal and slab structure.

A comparison of the synthetics produced for each of these five models to the data for event M1 at three stations is shown in Figure 10. The waveforms have been bandpass filtered to 0.01–0.1 Hz in order to increase the signal-to-noise ratio and accentuate the major phases (e.g., *P*, *sP*, and *S*). Overall, the ncMc model provides the most accurate prediction of the data on both vertical and horizontal components, with the best fits to *P*, *sP*, and *SH* phases at all distances (Figures 10 and 11). The FSa model provides a slightly improved fit to the *sP* and *SV* phases on the vertical component, but a poorer fit to all phases on the radial component (Figure 10). The ncM model provides a comparable fit to the ncMc model for the major phases on the radial component, with a slightly worse fit on the vertical component (Figure 10). The uppermost slab structure in the ncMc model, particularly the USL, is likely responsible for reproducing the observed horizontal waveforms that the simpler FSa model fails to accurately predict. Additionally, the recalculated *P* wave velocities of the ncMc model using the V_p/V_s ratio of the FSa model can be credited for improved predictions of the vertical component waveforms over the ncM model.

3.6. 2-D Velocity Modeling

To further investigate the shallow structure of the subducted South Cocos plate along the transition from flat to normal subduction, we produce synthetic seismograms with a 2-D finite difference wave propagation

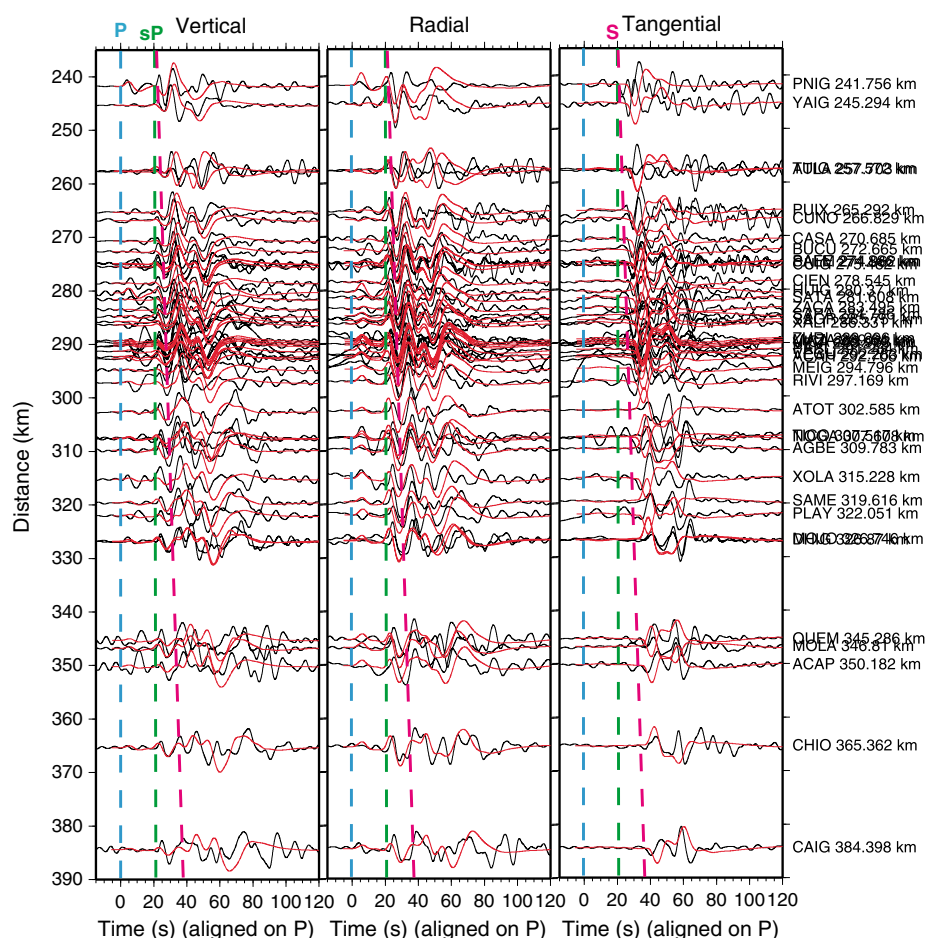


Figure 11. 1-D modeling results of event M1 for the ncMc velocity model filtered to 0.01–0.1 Hz. Data from MASE and SSN stations are in black, synthetics are in red. *P*, *sP*, and *S* phases are indicated by dashed lines. See Figure S4 in the supporting information for results plotted without station overlap.

algorithm for particular velocity and slab geometry models and compare these to the data for 16 events. As with the 1-D velocity modeling, we use source parameters from the CAP focal mechanisms (Table 1) to generate the synthetics. Models for the 16 events tested are oriented along 17 different profiles throughout the study region, concentrated across the USL, possible USL, and no USL zones in order to examine the validity of their boundaries (Figure 12a). Note that for event V2 both a NW-SE oriented profile and a E-W profile are modeled. All of the models investigated consist of *P* and *S* wave velocities from the ncMc model with subducted slab geometries estimated from the isodepth contours [Pérez-Campos *et al.*, 2008; Kim *et al.*, 2010, 2011; Melgar and Pérez-Campos, 2011]. The 2-D modeling results for all of the events tested are summarized in Figure 12b, where profile lines are colored to indicate locations of confirmed presence of the USL, possible presence of the USL, and lack of the USL. In general, the USL is shown to be present (or possibly present) across the entire width of the previously defined possible USL zone, from the coast to its northernmost estimated extent, although the profile furthest from the coast indicates only a small patch of the USL is present (event M2). Two parallel transects across this zone (events M9 and M3) are exceptions to this result, instead indicating that no USL is present. Additionally, the modeling results for the event M22 profile across this zone are inconclusive. Transects located to the north and east of the possible USL zone confirm that the USL is not present in these regions.

The preferred 2-D velocity model along the E-W profile for event V2 is presented in Figure 13 as an example. Data along this transect were recorded by OXNET and SSN stations. The USL in this model ends at the approximate eastern boundary of the possible USL (USL?) zone. The synthetics produced from this model (i.e., end1) are compared to the data from three stations in Figure 14. The model predicts the *P* and *sP* phases

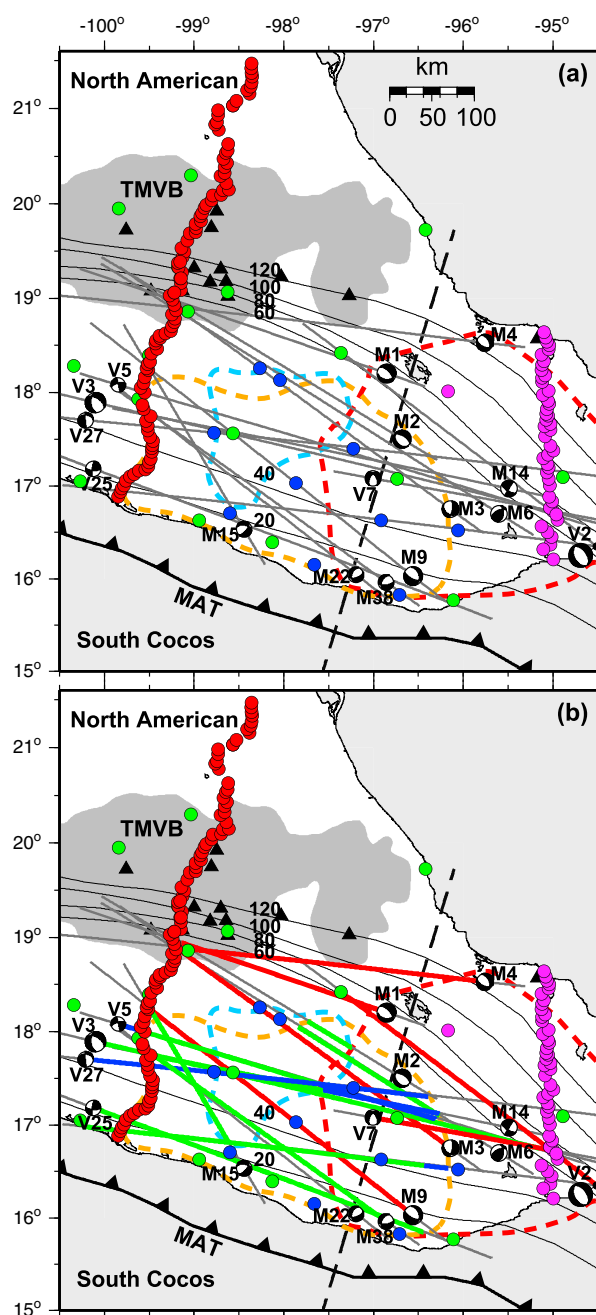


Figure 12. (a) Map of locations of 2-D velocity model cross sections (dark gray lines) for the 16 events modeled (focal mechanisms). Focal mechanisms are from this study. Thick dashed lines mark the boundaries of the USL (cyan), possibly USL (orange), and no USL (red) zones from Figure 5. (b) Same as (a) with cross-section lines colored to reflect 2-D modeling results. Confirmed presence of the USL is shown in green and possible presence of the USL is shown in blue. Red lines indicate a model without the USL provides the best representation of the data.

general, the correlation coefficients indicate that the end1 (i.e., preferred) model synthetics are better representations of the data than the end2 and no USL models. The correlation coefficients for the majority of the stations located along the profile clearly indicate that the end1 model synthetics fit the data better than those produced by the complete USL (i.e., ncMc) model on both the vertical and radial components. In comparison to the shifted boundary models, overall the correlation coefficients indicate increased accuracy for

reasonably well at all distances and the S wave at shorter distances. A later large amplitude phase, presumed to be an S wave multiple, is predicted reasonably well by the model at all stations.

In order to test the effect of the presence or absence of the USL and the location of its eastern lateral extent on the synthetic seismograms produced, we examine nine other models with the same velocity structure, including six which assess our model's sensitivity to the absolute location of the end of the USL: (1) USL continues across the entire width of model without an end (ncMc), (2) USL stops at approximate western boundary of the no USL zone (end2), (3) no USL present, thicker lower oceanic crust to compensate, (4) USL stops at approximate eastern boundary of the USL? zone shifted by 10 km to the west (end1+10), (5) USL? boundary shifted 25 km to the west (end1+25), (6) USL? boundary shifted 25 km to the east (end1-25), (7) USL? boundary shifted 30 km to the west (end1+30), (8) USL? boundary shifted 50 km to the west (end1+50), and (9) USL? boundary shifted 50 km to the east (end1-50). A comparison of the synthetics produced for each of the nine models and the preferred (end1) model to the data at three stations is shown in Figure 14. A ~40–53 s segment of the waveform after the S wave that includes the large amplitude, presumed S wave multiple illustrates the greatest variance among the models, indicating this phase is most sensitive to the USL. The synthetic waveform for each model is cross-correlated with the data for this segment. Due to the increased complexity of the waveforms observed on the radial component, we note that the correlation coefficients for all of the models are generally reduced relative to the vertical component and recommend weighing the vertical component results more heavily than the radial component. While there is some variance between the vertical and radial components, in

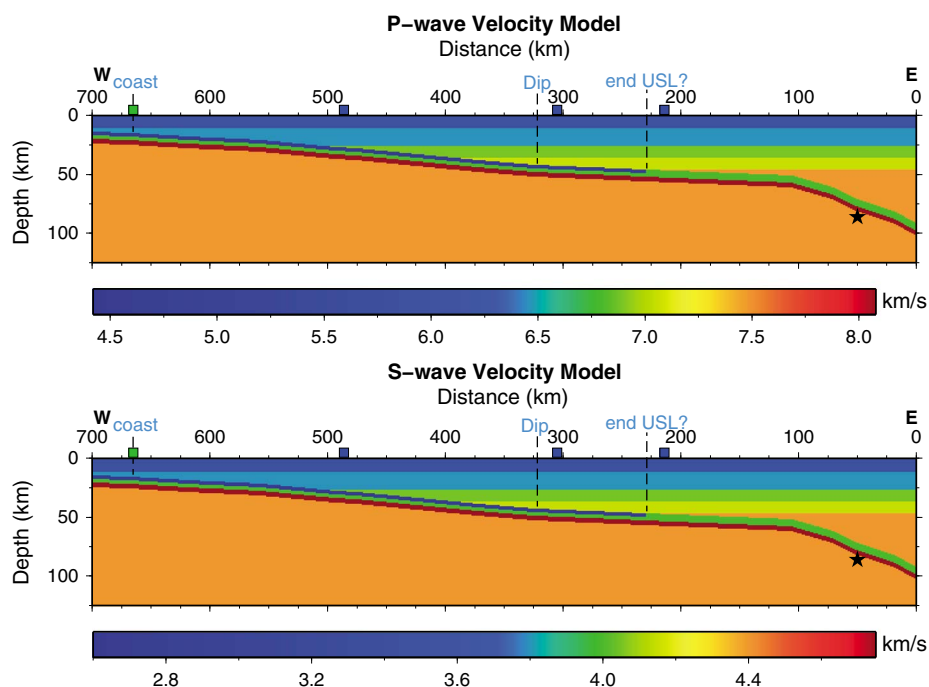


Figure 13. 2-D velocity model of the shallow subduction zone structure across the OXNET (blue squares) and SSN (green square) arrays along the E-W profile for event V2 in Figure 12. *P* and *S* wave velocities are from the ncMc model. Subducted slab shape is estimated from the isodepth contours. Locations of the approximate end of the possible USL (USL?) zone, the sharp transition in slab dip, and the coastline are indicated for reference. The location of event V2 used in the modeling is shown by the black star.

synthetics produced with boundary shifts of 10–30 km to the west relative to those produced by the end1 model. On the other hand, boundary shifts of 25–50 km to the east produce worse fits to the data than the end1 model. These results suggest the confirmed presence of the USL to a location 30 km west of the eastern USL? boundary and the possible presence of the USL between this location and the USL? boundary (as indicated in Figure 12b).

The preferred 2-D velocity model along the event M2 profile and a comparison of the synthetics produced for each of the models tested to the data are shown in Figures S5 and S6, respectively, as an additional example.

4. Discussion

The abrupt end of the TMVB coupled with the interruption of arc volcanism near the transition from flat to normal subduction in eastern central Mexico suggests a possible slab tear located within the subducted South Cocos plate. In this study, we provide further evidence for such a tear based on seismic observations, source mechanism analysis, and modeling of the velocity structure of the subduction zone. From estimating the lateral variation in slab dip using Wadati-Benioff zone seismicity, we find a sharp increase in slab dip indicative of a possible tear in the South Cocos plate. Due to the short distance over which this increase in dip occurs (~50 km), it is unlikely to be accommodated by a smooth contortion of the slab, as suggested by Pardo and Suárez [1995]. The location of this sharp transition in slab dip near the end of the TMVB may have important implications for the observed gap in arc volcanism. With the increase in slab dip eastward from the TMVB, it would be expected that the arc volcanism would shift trenchward, following the slab, but the lack of observed volcanism instead suggests that a slab source for melt generation could be missing beneath this area. A tear in the South Cocos slab that begins downdip and extends trenchward to <100 km depth (i.e., the point of decompression melting) could explain the suggested lack of a slab source. Alternatively, the truncation of the South Cocos slab observed to the east by the Yucatán slab, which restricts flow in the mantle wedge, may also explain the unusual configuration of arc volcanism in the region [Kim *et al.*, 2011; Chen and Clayton, 2012].

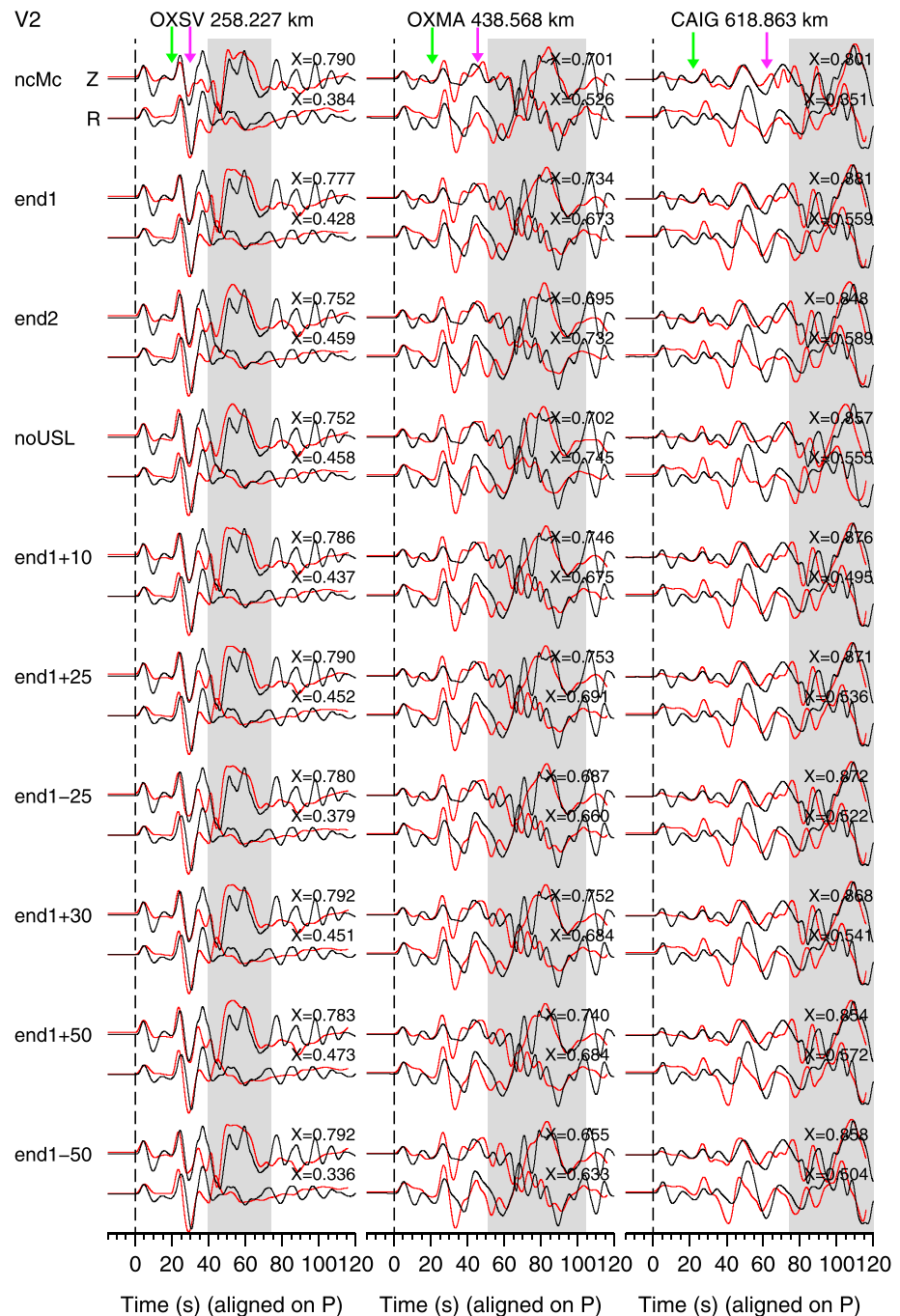


Figure 14. Comparison of 2-D modeling results of event V2 along the E-W profile for 10 different models at three stations, filtered to 0.01–0.1 Hz. Data are in black, synthetics are in red. Vertical (Z) and radial (R) components are shown. P (dashed line), sP (green arrow), and S (pink arrow) arrivals are indicated. The primary variance among the models was the USL: ncMc = USL continues across entire width of model without an end; end1 = USL stops at approximate eastern boundary of the USL zone; end2 = USL stops at approximate western boundary of the no USL zone; noUSL = no USL present, thicker lower oceanic crust to compensate; end1+10, end1+25, end1+30, and end1+50 = USL? boundary shifted 10 km, 25 km, 30 km, and 50 km, respectively, to the west; end1–25 and end1–50 = USL? boundary shifted 25 km and 50 km, respectively, to the east. Segment of waveform illustrating greatest variance among the models is shaded gray. Cross-correlation coefficients (X) for each model with the data for the selected segment are shown.

Examination of the eastern lateral extent of the USL shows a complex pattern that cannot be mapped as a single linear feature, as was done by *Dougherty et al.* [2012] for the western extent. The observed boundary between the USL and no USL zones that is coincident with the end of the TMVB suggests a change in plate structure here and could indicate a possible tear in the South Cocos slab. East of here there is a transitional, weakening USL zone, evident in the overlapping possible USL and no USL regions closer to the coast. This patchy, petering out of the USL in the updip portion of the slab further implies that the possible slab tear is currently concentrated downdip, as the hydrous minerals and potential pore fluid of the USL would not be maintained across a break in the slab at shallower depths. This mapping of the USL extent contradicts similar mapping by *Song et al.* [2009], which showed no observed USL in the region of our USL zone. The events analyzed by *Song et al.* [2009] in this region of overlap were recorded by a single station prior to the MASE array deployment, while we utilize data from multiple arrays with events recorded by a minimum of 24 (and up to 94) stations. The increased quantity and quality of our data relative to that of *Song et al.* [2009] likely accounts for the discrepancy in results and favors our mapping of the USL. Additionally, the 2-D finite difference modeling confirmed the location of the USL across the entire width of the USL and possible USL zones, further solidifying our mapping.

The intraslab seismicity patterns observed across the study region provide further evidence for a possible tear in the South Cocos slab. The margin of a zone of decreased seismicity located to the west of the sharp transition in slab dip is coincident with both the end of the TMVB and the boundary between the USL and no USL zones. The decreased seismicity of this zone suggests a change in plate structure, and its coincidence with the TMVB and USL boundaries further suggests that this change could indicate a tear in the slab. If the slab was undergoing plate flexure along a smooth contortion instead, we would expect an increase in seismicity, not a decrease [*McCorry et al.*, 2012]. The clustering of events within this zone (bins 12 and 13) may imply focusing of stress from a tear that is propagating updip from a deeper point, as has been observed for slab tears in other subduction zones [*Gutscher et al.*, 1999; *Miller et al.*, 2004; *Clark et al.*, 2008; *Meighan et al.*, 2013b]. The abrupt increase in depth at the point of rotation of the downdip seismicity band near the end of the TMVB also suggests a structural change indicative of a possible slab tear.

Focal mechanisms of the intraslab seismicity elucidate the nature of the flat to normal transition in slab dip beyond that of the epicentral ISC catalog locations. The observed decrease in depth of events from the shallowly dipping to the more steeply dipping portion of the slab in both the GCMT and SSN CMT catalog data and the CAP focal mechanisms indicates a change in stress distribution across this region. The deeper events on the shallowly dipping segment may be due to a localized stress concentration as a result of the steeper adjacent segment [*Pacheco and Singh*, 2010] and/or downdip tearing of the slab. Both of these scenarios could produce a vertical column of seismicity like that suggested based on the cross sections of the CAP focal mechanisms. Such a column has been observed along slab tears in the southern Lesser Antilles [*Clark et al.*, 2008], the northeast Caribbean [*Meighan et al.*, 2013b], and Tonga [*Millen and Hamburger*, 1998]. In eastern central Mexico, the intraslab seismicity is generally sparse, making it difficult to conclude that a vertical column of seismicity exists here, yet the implications of the possibility are relevant to our discussion.

In addition to the patterns in their spatial distribution, the orientations of the focal mechanisms also provide evidence for a possible slab tear. While normal faulting mechanisms are generally predominant, the orientations of these mechanisms are highly variable near the sharp transition in slab dip, suggesting a complex stress distribution [*Pardo and Suárez*, 1995; *Rebollar et al.*, 1999]. The observed concentration of strike-slip mechanisms in this region indicates further complexity of the stress field. Such variation in stress orientations suggests that the earthquakes are either accommodating the strain that is necessary for the slab to fail and tear or failure of the slab has already taken place and the seismicity is the result of faulting as adjacent mantle is drawn into the gap [*Miller et al.*, 2004]. The strike-slip focal mechanisms may be accommodating the shear motion that is thought to be associated with the slab tearing process [*Burbach et al.*, 1984; *Rosenbaum et al.*, 2008; *Meighan et al.*, 2013b; *Vargas and Mann*, 2013]. This range of earthquake mechanisms and orientations observed near the possible tear in the South Cocos slab is consistent with observations at slab tears in other subduction zones [e.g., *Russo et al.*, 1993; *Bilich et al.*, 2001]. Additionally, the approximate alignment of steeply dipping focal planes for some CAP mechanisms along the strike of the change in dip line suggest tearing of the slab per *Gutscher et al.*'s [1999] classification of "tearing events."

The ~50–75 km wide offset between the eastern end of the TMVB and the sharp transition in slab dip suggests the existence of a downdip tear zone which encompasses the various seismic observations

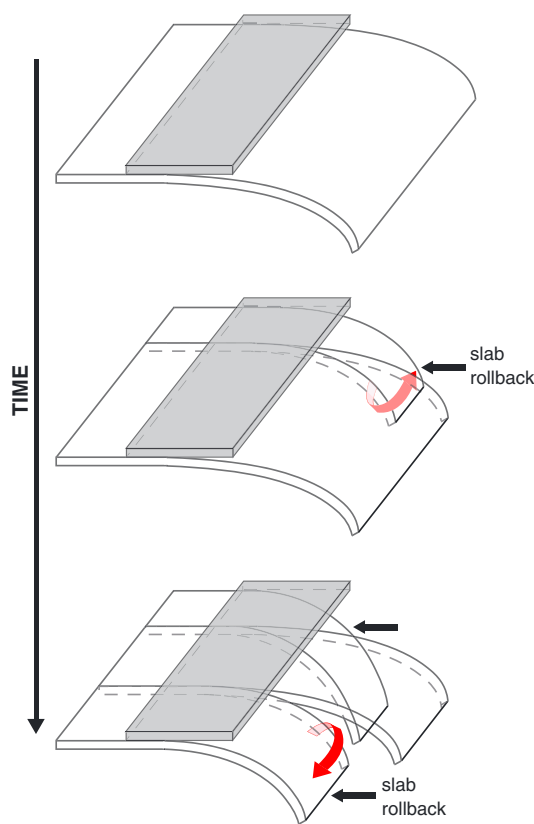


Figure 15. 3-D schematic of the slab rollback process and plate tearing through time. (top) Start with a flat slab. (middle) Slab rollback begins on only a segment of the plate; first plate tear develops, allowing mantle flow through the gap (red arrow). (bottom) Slab rollback continues, and a second segment of the plate begins rolling back; second plate tear develops, allowing further mantle flow between the segments.

flat to normal subduction in Chile, where a gap in fast velocities at depths of 220–340 km suggests a local tear in the downdip portion of the slab [Pesicek *et al.*, 2012]. The lack of surface volcanism further implies that any asthenospheric mantle material which may be flowing through the tear is not rising to a shallow enough depth to have an effect on the overriding plate [Miller *et al.*, 2009].

The possible tear in the South Cocos slab may be the result of the subduction of several parallel ridges of seamounts off the coast of Oaxaca. Seamount subduction is a common process that is often related to large earthquake ruptures, although the role of seamounts as asperities or barriers to rupture propagation is controversial [see, e.g., Cloos, 1992; Scholz and Small, 1997; Wang and Bilek, 2011; Kopp, 2013; Yang *et al.*, 2013, and references therein]. The subduction of seafloor heterogeneities, which induce an abrupt variation of the mechanical properties of the oceanic plate, may provide a preferred location to initiate a tear within the slab [Chatelain *et al.*, 1992; Bonnardot *et al.*, 2009; Mason *et al.*, 2010]. These inhomogeneities may reduce the strength of the lithosphere resulting in a weak zone along which a tear will propagate [Hale *et al.*, 2010]. In the case of seamounts, this weak zone is located along the margin of the strengthened lithosphere (i.e., along the chain or ridge) [Hale *et al.*, 2010], where seamount-parallel faults have been observed offshore central Mexico [Kanjorski, 2003]. The eastern margin of the Puerto Escondido seamount cluster is located near 97.5°W at the MAT, coincident with the sharp transition in slab dip. This spatial correlation supports seamount subduction as a cause of the possible slab tear. In addition to (or instead of) this proposed cause, the accommodation of a considerable amount of strain in the slab due to the abrupt variation in geometry (i.e., sharp transition in slab dip) may promote tearing [Miller *et al.*, 2004, 2005; Yang *et al.*, 2009].

In conjunction with the tear in western central Mexico [Dougherty *et al.*, 2012; Stubbailo *et al.*, 2012], the possible slab tear in the South Cocos plate proposed here may play an important role in the rollback

presented here. The western margin of this tear zone is defined by the termination of the TMVB and its coincidence with the boundary between the USL and no USL regions and the limit of an area of decreased intraslab seismicity, indicating this margin is a marked structural boundary in the downdip portion of the slab. The eastern margin of the tear zone is delineated by the sharp transition in slab dip and, based on the spatial distribution and orientations of the focal mechanisms analyzed in this study, the locus of active tearing of the South Cocos slab is proposed to occur along here. The continuation of a weakening USL zone in the updip portion of the slab across this tear zone and the sharp transition in slab dip demonstrates that the presence of the USL is not controlled simply by geometry, consistent with observations in western central Mexico [Dougherty *et al.*, 2012]. Rather, the presence of the USL is strongly controlled by the structure of the South Cocos slab, which is still continuous in the shallow updip region.

The lack of surficial expression of the possible tear (e.g., rifting or magmatism) implies that it is a less developed or young feature and supports the theory that it is currently localized to the downdip, aseismic portion of the slab. *P* wave tomography shows a gap in the imaged slab at the eastern end of the TMVB at 380 km depth [Gorbatov and Fukao, 2005], which is interpreted as a tear in the slab. A similar observation has been made along the transition from

process by allowing the slab to rollback in segments, resulting in observed along trench variations in slab dip (Figure 15). As slab rollback begins on only a segment of the plate, the first slab tear develops, allowing mantle flow through the gap. Over time, slab rollback continues, steepening the initial segment and inducing rollback in another segment of the plate, where a second slab tear develops, allowing further mantle flow between the segments. This steepening of the slab during rollback pushes material laterally from underneath the slab around an edge and into the overlying mantle wedge [Russo and Silver, 1994; Schellart, 2004; Jadamec and Billen, 2010]. This flow is presumably currently accommodated by the gap between the North Cocos and Rivera plates [Soto et al., 2009]. The proposed tears in the plate would significantly shortcut this process. Additionally, the toroidal flow through the tear introduces less dense and viscous asthenosphere material into the mantle wedge, promoting rapid rollback of the slab segment [Schellart et al., 2007; Soto et al., 2009].

5. Conclusions

The nature of the transition from flat to normal subduction in eastern central Mexico is interrogated using intraslab seismicity patterns, an analysis of *P* waveform complexities, and 1-D and 2-D waveform modeling techniques. The results show that the subducted South Cocos plate is a complicated, multilayered structure with a thin USL atop the slab. The lateral extent of this USL is marked by a boundary between the USL and no USL zones, followed by a diffuse weakening USL region closer to the coast. A sharp transition in slab dip near the abrupt end of the TMVB suggests a possible tear in the South Cocos slab. The coincidence of the boundary between the USL and no USL zones with the margin of a zone of decreased seismicity along this change in dip and the end of the TMVB implies a change in structure which we interpret as evidence of a possible tear. Additional observed intraslab seismicity patterns of clustering, sudden increase in depth, variable focal mechanism orientations and faulting types, and alignment of source mechanisms along the sharp transition in slab dip further support this conclusion. We propose the subduction of parallel ridges of seamounts and/or stress due to the abrupt change in geometry as potential causes of the possible slab tear in the South Cocos plate. Further imaging of the subduction zone structure with denser station coverage over the downdip aseismic portion of the slab may provide a clearer picture of the possible tear at depth.

Acknowledgments

MASE and VEOX data are available at the IRIS DMC under the network code TO. Researchers should contact Michael Brudzinski for OXNET data and Carlos M. Valdes Gonzalez for SSN waveform data. The SSN event catalog is accessible from the Servicio Sismológico Nacional website (<http://www.ssn.unam.mx/>). The SSN CMT catalog is available on the Mexican CMT Project website (<http://laxdoru.igeofcu.unam.mx/cmt/>). The ISC Bulletin event catalog is accessible from the International Seismological Centre website (<http://www.isc.ac.uk/>). This study was supported in part by the Gordon and Betty Moore Foundation through the Tectonics Observatory at California Institute of Technology. This is contribution 256 from the Caltech Tectonics Observatory. We are grateful to Michael Brudzinski, Enrique Cabral-Cano, and Alejandra Arciniega-Ceballos for making the OXNET waveform data available. We thank Arturo Iglesias for providing the Servicio Sismológico Nacional event catalog and Ting Chen for the slab isodepth contour lines. We also thank Editor Robert Nowack, the Associate Editor, Sebastiano D'Amico, and an anonymous reviewer for helpful comments, which improved the manuscript.

References

- Abd, D. L., K. M. Fischer, G. A. Abers, M. Protti, V. Gonzalez, and W. Strauch (2010), Constraints on upper mantle anisotropy surrounding the Cocos slab from SK(K)S splitting, *J. Geophys. Res.*, *115*, B06316, doi:10.1029/2009JB006710.
- Alberto, C. A. O. (2010), Caracterización de la geometría de la zona benioff con una red densa de banda ancha en el istmo de Tehuantepec, PhD thesis, Natl. Auton. Univ. of Mex., Mexico City, Mexico.
- Bandy, W., C. Mortera-Gutierrez, J. Urrutia-Fucugauchi, and T. W. C. Hilde (1995), The subducted Rivera-Cocos plate boundary: Where is it, what is it, and what is its relationship to the Colima rift?, *Geophys. Res. Lett.*, *22*, 3075–3078.
- Bandy, W. L., T. W. C. Hilde, and C.-Y. Yan (2000), The Rivera-Cocos plate boundary: Implications for Rivera-Cocos relative motion and plate fragmentation, in *Cenozoic Tectonics and Volcanism of Mexico*, vol. 334, edited by H. Delgado-Granados, G. Aguirre-Diaz, and J. M. Stock, pp. 1–28, Geol. Soc. Am. Spec. Pap., GSA, Boulder, Colo.
- Batiza, R., T. L. Smith, and Y. Niu (1989), Geological and petrologic evolution of seamounts near the EPR based on submersible and camera study, *Mar. Geophys. Res.*, *11*, 169–236.
- Bilich, A., C. Frohlich, and P. Mann (2001), Global seismicity characteristics of subduction-to-strike-slip transitions, *J. Geophys. Res.*, *106*, 19,443–19,452.
- Bonnardot, M.-A., M. Régnier, C. Christova, E. Ruellan, and E. Tric (2009), Seismological evidence for a slab detachment in the Tonga subduction zone, *Tectonophysics*, *464*, 84–99, doi:10.1016/j.tecto.2008.10.011.
- Brudzinski, M. R., H. R. Hinojosa-Prieto, K. M. Schlanser, E. Cabral-Cano, A. Arciniega-Ceballos, O. Diaz-Molina, and C. DeMets (2010), Nonvolcanic tremor along the Oaxaca segment of the Middle America subduction zone, *J. Geophys. Res.*, *115*, B00A23, doi:10.1029/2008JB006061.
- Burbach, G. V., C. Frohlich, W. D. Pennington, and T. Matumoto (1984), Seismicity and tectonics of the subducted Cocos plate, *J. Geophys. Res.*, *89*, 7719–7735.
- Burkett, E. R., and M. I. Billen (2010), Three-dimensionality of slab detachment due to ridge-trench collision: Laterally simultaneous boudinage versus tear propagation, *Geochem. Geophys. Geosyst.*, *11*, Q11012, doi:10.1029/2010GC003286.
- Cahill, T. A., and B. L. Isacks (1992), Seismicity and shape of the subducted Nazca plate, *J. Geophys. Res.*, *97*, 17,503–17,529.
- Chatelain, J.-L., P. Molnar, R. Prévot, and B. Isacks (1992), Detachment of part of the downgoing slab and uplift of the New Hebrides (Vanuatu) Islands, *Geophys. Res. Lett.*, *19*, 1507–1510.
- Chen, T., and R. W. Clayton (2012), Structure of central and southern Mexico from velocity and attenuation tomography, *J. Geophys. Res.*, *117*, B09302, doi:10.1029/2012JB009233.
- Clark, S. A., M. Sobiesiak, C. A. Zelt, M. B. Magnani, M. S. Miller, M. J. Bezada, and A. Levander (2008), Identification and tectonic implications of a tear in the South American plate at the southern end of the Lesser Antilles, *Geochem. Geophys. Geosyst.*, *9*, Q11004, doi:10.1029/2008GC002084.
- Cloos, M. (1992), Thrust-type subduction-zone earthquakes and seamount asperities: A physical model for seismic rupture, *Geology*, *20*, 601–604.
- D'Amico, S., B. Orecchio, D. Presti, L. Zhu, and R. B. Herrmann (2010), Broadband waveform inversion of moderate earthquakes in the Messina Straits, southern Italy, *Phys. Earth Planet. Inter.*, *179*, 97–106, doi:10.1016/j.pepi.2010.01.012.

- D'Amico, S., B. Orecchio, D. Presti, A. Gervasi, L. Zhu, I. Guerra, G. Neri, and R. B. Herrmann (2011), Testing the stability of moment tensor solutions for small earthquakes in the Calabro-Peloritan Arc region (southern Italy), *Boll. Geofis. Teor. Appl.*, **52**, 283–298, doi:10.4430/bgta0009.
- DeMets, C., and S. Traylen (2000), Motion of the Rivera plate since 10 Ma relative to the Pacific and North American plates and the mantle, *Tectonophysics*, **318**, 119–159.
- DeMets, C., R. G. Gordon, and D. F. Argus (2010), Geologically current plate motions, *Geophys. J. Int.*, **181**, 1–80, doi:10.1111/j.1365-246X.2009.04491.x.
- Dougherty, S. L., R. W. Clayton, and D. V. Helmberger (2012), Seismic structure in central Mexico: Implications for fragmentation of the subducted Cocos plate, *J. Geophys. Res.*, **117**, B09316, doi:10.1029/2012JB009528.
- Dziewonski, A. M., T.-A. Chou, and J. H. Woodhouse (1981), Determination of earthquake source parameters from waveform data for studies of global and regional seismicity, *J. Geophys. Res.*, **86**, 2825–2852, doi:10.1029/JB086iB04p02825.
- Ekström, G., M. Nettles, and A. M. Dziewonski (2012), The global CMT project 2004–2010: Centroid-moment tensors for 13,017 earthquakes, *Phys. Earth Planet. Inter.*, **200**, 1–9, doi:10.1016/j.pepi.2012.04.002.
- Ferrari, L. (2004), Slab detachment control on mafic volcanic pulse and mantle heterogeneity in Central Mexico, *Geology*, **32**, 77–80, doi:10.1130/G19887.1.
- Ferrari, L., T. Tagami, M. Eguchi, M. T. Orozco-Esquivel, C. M. Petrone, J. Jacobo-Albarrán, and M. López-Martínez (2005), Geology, geochronology and tectonic setting of late Cenozoic volcanism along the southwestern Gulf of Mexico: The Eastern Alkaline Province revisited, *J. Volcanol. Geotherm. Res.*, **146**, 284–306, doi:10.1016/j.jvolgeores.2005.02.004.
- Ferrari, L., T. Orozco-Esquivel, V. Manea, and M. Manea (2011), The dynamic history of the Trans-Mexican Volcanic Belt and the Mexico subduction zone, *Tectonophysics*, **522**, 122–149, doi:10.1016/j.tecto.2011.09.018.
- Franco, S. I., V. Kostoglodov, K. M. Larson, V. C. Manea, M. Manea, and J. A. Santiago (2005), Propagation of the 2001–2002 silent earthquake and interplate coupling in the Oaxaca subduction zone, Mexico, *Earth Planets Space*, **57**, 973–985.
- Fryer, P., N. Becker, B. Appelgate, F. Martinez, M. Edwards, and G. Fryer (2003), Why is the Challenger Deep so deep?, *Earth Planet. Sci. Lett.*, **211**, 259–269.
- Furumura, T., and S. K. Singh (2002), Regional wave propagation from Mexican subduction zone earthquakes: The attenuation functions for interplate and inslab events, *Bull. Seismol. Soc. Am.*, **92**, 2110–2125, doi:10.1785/0120010278.
- Gasparon, M., G. Rosenbaum, J. Wijbrans, and P. Manetti (2009), The transition from subduction arc to slab tearing: Evidence from Capraia Island, northern Tyrrhenian Sea, *J. Geodyn.*, **47**, 30–38.
- Gómez-Tuena, A., M. T. Orozco-Esquivel, and L. Ferrari (2007), Igneous petrogenesis of the Trans-Mexican Volcanic Belt, in *Geology of Mexico: Celebrating the Centenary of the Geological Society of México*, vol. 422, edited by S. A. Alaniz-Alvarez and A. F. Nieto-Samaniego, pp. 129–181, Spec. Pap. Geol. Soc. Am., GSA, Boulder, Colo.
- Gorbatov, A., and Y. Fukao (2005), Tomographic search for missing link between the ancient Farallon subduction and the present Cocos subduction, *Geophys. J. Int.*, **160**, 849–854, doi:10.1111/j.1365-246X.2005.02507.x.
- Govers, R., and M. J. R. Wortel (2005), Lithosphere tearing at STEP faults: Response to edges of subduction zones, *Earth Planet. Sci. Lett.*, **236**, 505–523, doi:10.1016/j.epsl.2005.03.022.
- Gutscher, M.-A., J. Malavieille, S. Lallemand, and J.-Y. Collot (1999), Tectonic segmentation of the North Andean margin: Impact of the Carnegie Ridge collision, *Earth Planet. Sci. Lett.*, **168**, 255–270.
- Hale, A. J., K.-D. Gottschaldt, G. Rosenbaum, L. Bourgoign, M. Bauchy, and H. Mühlhaus (2010), Dynamics of slab tear faults: Insights from numerical modelling, *Tectonophysics*, **483**, 58–70, doi:10.1016/j.tecto.2009.05.019.
- Husker, A., and P. M. Davis (2009), Tomography and thermal state of the Cocos plate subduction beneath Mexico City, *J. Geophys. Res.*, **114**, B04306, doi:10.1029/2008JB006039.
- International Seismological Centre (2011), *On-line Bulletin*, Int. Seis. Cent., Thatcham, U. K. [Available at <http://www.isc.ac.uk>]
- Isacks, B. L., and M. Barazangi (1977), Geometry of Benioff zones: Lateral segmentation and downwards bending of the subducted lithosphere, in *Island Arcs, Deep Sea Trenches and Back-Arc Basins, Maurice Ewing Series*, vol. 1, edited by M. Talwani and W. C. Pitman, pp. 99–114, AGU, Washington, D. C.
- Jadamec, M. A., and M. I. Billen (2010), Reconciling surface plate motions with rapid three-dimensional mantle flow around a slab edge, *Nature*, **465**, 338–341, doi:10.1038/nature09053.
- Johnston, S. T., and D. J. Thorkelson (1997), Cocos-Nazca slab window beneath central America, *Earth Planet. Sci. Lett.*, **146**, 465–474.
- Kanjorski, N. M. (2003), Cocos plate structure along the Middle America subduction zone off Oaxaca and Guerrero, Mexico: Influence of subducting plate morphology on tectonics and seismicity, PhD thesis, Univ. of Calif., San Diego, Calif.
- Kim, Y., R. W. Clayton, and J. M. Jackson (2010), Geometry and seismic properties of the subducting Cocos plate in Central Mexico, *J. Geophys. Res.*, **115**, B06310, doi:10.1029/2009JB006942.
- Kim, Y., R. W. Clayton, and F. Keppie (2011), Evidence of a collision between the Yucatán Block and Mexico in the Miocene, *Geophys. J. Int.*, **187**, 989–1000, doi:10.1111/j.1365-246X.2011.05191.x.
- Kim, Y., R. W. Clayton, P. D. Asimow, and J. M. Jackson (2013), Generation of talc in the mantle wedge and its role in subduction dynamics in Central Mexico, *Earth Planet. Sci. Lett.*, **384**, 81–87, doi:10.1016/j.epsl.2013.10.006.
- Klitgord, K. D., and J. Mammertckx (1982), Northern East Pacific Rise: Magnetic anomaly and bathymetric framework, *J. Geophys. Res.*, **87**, 6725–6750.
- Kneller, E. A., and P. E. van Keken (2008), Effect of three-dimensional slab geometry on deformation in the mantle wedge: Implications for shear wave anisotropy, *Geochim. Geophys. Res.*, **9**, Q01003, doi:10.1029/2007GC001677.
- Kopp, H. (2013), Invited review paper: The control of subduction zone structural complexity and geometry on margin segmentation and seismicity, *Tectonophysics*, **589**, 1–16, doi:10.1016/j.tecto.2012.12.037.
- Lin, J.-Y., S.-K. Hsu, and J.-C. Sibuet (2004), Melting features along the Ryukyu slab tear, beneath the Southwestern Okinawa trough, *Geophys. Res. Lett.*, **31**, L19607, doi:10.1029/2004GL020862.
- Lonsdale, P. (2005), Creation of the Cocos and Nazca plates by fission of the Farallon plate, *Tectonophysics*, **404**, 237–264, doi:10.1016/j.tecto.2005.05.011.
- Macías, J. L. (2007), Geology and eruptive history of some active volcanoes of Mexico, in *Geology of México: Celebrating the Centenary of the Geological Society of México*, vol. 422, edited by S. A. Alaniz-Alvarez and A. F. Nieto-Samaniego, pp. 183–232, Spec. Pap. Geol. Soc. Am., GSA, Boulder, Colo.
- Mammertckx, J., and K. D. Klitgord (1982), Northern East Pacific Rise: Evolution from 25 m.y. B.P. to the present, *J. Geophys. Res.*, **87**, 6751–6759.
- Manea, V., and M. Gurnis (2007), Subduction zone evolution and low viscosity wedges and channels, *Earth Planet. Sci. Lett.*, **264**, 22–45, doi:10.1016/j.epsl.2007.08.030.

- Manea, V. C., M. Manea, V. Kostoglodov, C. A. Currie, and G. Sewell (2004), Thermal structure, coupling and metamorphism in the Mexican subduction zone beneath Guerrero, *Geophys. J. Int.*, *158*, 775–784, doi:10.1111/j.1365-246X.2004.02325.x.
- Manea, V. C., M. Manea, V. Kostoglodov, and G. Sewell (2006), Intralab seismicity and thermal stress in the subducted Cocos plate beneath central Mexico, *Tectonophysics*, *420*, 389–408, doi:10.1016/j.tecto.2006.03.029.
- Manea, V. C., M. Manea, and L. Ferrari (2013), A geodynamical perspective on the subduction of Cocos and Rivera plates beneath Mexico and Central America, *Tectonophysics*, *609*, 56–81, doi:10.1016/j.tecto.2012.12.039.
- MASE (2007), Meso America subduction experiment, Caltech, dataset, doi:10.7909/C3RN35SP.
- Mason, W. G., L. Moresi, P. G. Betts, and M. S. Miller (2010), Three-dimensional numerical models of the influence of a buoyant oceanic plateau on subduction zones, *Tectonophysics*, *483*, 71–79, doi:10.1016/j.tecto.2009.08.021.
- McClain, J. S., and M. A. Wright (1990), The morphology and structure of the West O’Gorman Fracture Zone, *Mar. Geophys. Res.*, *12*, 317–328.
- McCrory, P. A., J. L. Blair, F. Waldhauser, and D. H. Oppenheimer (2012), Juan de Fuca slab geometry and its relation to Wadati-Benioff zone seismicity, *J. Geophys. Res.*, *117*, B09306, doi:10.1029/2012JB009407.
- Meighan, H. E., J. Pulliam, U. ten Brink, and A. M. López-Venegas (2013a), Seismic evidence for a slab tear at the Puerto Rico Trench, *J. Geophys. Res. Solid Earth*, *118*, 2915–2923, doi:10.1002/jgrb.50227.
- Meighan, H. E., U. ten Brink, and J. Pulliam (2013b), Slab tears and intermediate-depth seismicity, *Geophys. Res. Lett.*, *40*, 4244–4248, doi:10.1002/grl.50830.
- Melgar, D., and X. Pérez-Campos (2011), Imaging the Moho and subducted oceanic crust at the Isthmus of Tehuantepec, Mexico, from receiver functions, *Pure Appl. Geophys.*, *168*, 1449–1460, doi:10.1007/s00024-010-0199-5.
- Millen, D. W., and M. W. Hamburger (1998), Seismological evidence for tearing of the Pacific plate at the northern termination of the Tonga subduction zone, *Geology*, *26*, 659–662.
- Miller, M. S., B. L. N. Kennett, and G. S. Lister (2004), Imaging changes in morphology, geometry, and physical properties of the subducting Pacific plate along the Izu-Bonin-Mariana arc, *Earth Planet. Sci. Lett.*, *224*, 363–370, doi:10.1016/j.epsl.2004.05.018.
- Miller, M. S., A. Gorbatov, and B. L. N. Kennett (2005), Heterogeneity within the subducting Pacific slab beneath the Izu-Bonin-Mariana arc: Evidence from tomography using 3D ray tracing inversion techniques, *Earth Planet. Sci. Lett.*, *235*, 331–342, doi:10.1016/j.epsl.2005.04.007.
- Miller, M. S., A. Gorbatov, and B. L. N. Kennett (2006), Three-dimensional visualization of a near-vertical slab tear beneath the Southern Mariana arc, *Geochem. Geophys. Geosyst.*, *7*, Q06012, doi:10.1029/2005GC001110.
- Miller, M. S., A. Levander, F. Niu, and A. Li (2009), Upper mantle structure beneath the Caribbean-South American plate boundary from surface wave tomography, *J. Geophys. Res.*, *114*, B01312, doi:10.1029/2007JB005507.
- Nelson, S. A., E. Gonzalez-Caver, and T. K. Kyser (1995), Constraints on the origin of alkaline and calc-alkaline magmas from the Tuxtla Volcanic Field, Veracruz, Mexico, *Contrib. Mineral. Petrol.*, *122*, 191–211.
- Nolet, G. (2009), Slabs do not go gently, *Science*, *324*, 1152–1153, doi:10.1126/science.1174664.
- Pacheco, J. F., and S. K. Singh (2010), Seismicity and state of stress in Guerrero segment of the Mexican subduction zone, *J. Geophys. Res.*, *115*, B01303, doi:10.1029/2009JB006453.
- Pardo, M., and G. Suárez (1995), Shape of the subducted Rivera and Cocos plates in Southern Mexico: Seismic and tectonic implications, *J. Geophys. Res.*, *100*, 12,357–12,373.
- Pérez-Campos, X., Y. Kim, A. Husker, P. M. Davis, R. W. Clayton, A. Iglesias, J. F. Pacheco, S. K. Singh, V. C. Manea, and M. Gurnis (2008), Horizontal subduction and truncation of the Cocos Plate beneath Central Mexico, *Geophys. Res. Lett.*, *35*, L18303, doi:10.1029/2008GL035127.
- Pesicek, J. D., E. R. Engdahl, C. H. Thurber, H. R. DeShon, and D. Lange (2012), Mantle subducting slab structure in the region of the 2010 M8.8 Maule earthquake (30–40°S), Chile, *Geophys. J. Int.*, *191*, 317–324, doi:10.1111/j.1365-246X.2012.05624.x.
- Peyton, V., V. Levin, J. Park, M. Brandon, J. Lees, E. Gordeev, and A. Ozerov (2001), Mantle flow at a slab edge: Seismic anisotropy in the Kamchatka region, *Geophys. Res. Lett.*, *28*, 379–382.
- Protti, M., F. Gündel, and K. McNally (1994), The geometry of the Wadati-Benioff zone under southern Central America and its tectonic significance: Results from a high-resolution local seismograph network, *Phys. Earth Planet. Inter.*, *84*, 271–287.
- Rebollar, C. J., V. H. Espindola, A. Uribe, A. Mendoza, and A. Pérez-Vertti (1999), Distributions of stresses and geometry of the Wadati-Benioff zone under Chiapas, Mexico, *Geofis. Int.*, *38*, 95–106.
- Rosenbaum, G., M. Gasparon, F. P. Lucente, A. Peccerillo, and M. S. Miller (2008), Kinematics of slab tear faults during subduction segmentation and implications for Italian magmatism, *Tectonics*, *27*, TC2008, doi:10.1029/2007TC002143.
- Russo, R. M., and P. G. Silver (1994), Trench-parallel flow beneath the Nazca plate from seismic anisotropy, *Science*, *263*, 1105–1111.
- Russo, R. M., R. C. Speed, E. A. Okal, J. B. Shepherd, and K. C. Rowley (1993), Seismicity and tectonics of the Southeastern Caribbean, *J. Geophys. Res.*, *98*, 14,299–14,319.
- Schellart, W. P. (2004), Kinematics of subduction and subduction-induced flow in the upper mantle, *J. Geophys. Res.*, *109*, B07401, doi:10.1029/2004JB002970.
- Schellart, W. P., J. Freeman, D. R. Stegman, L. Moresi, and D. May (2007), Evolution and diversity of subduction zones controlled by slab width, *Nature*, *446*, 308–311, doi:10.1038/nature05615.
- Scholz, C. H., and C. Small (1997), The effect of seamount subduction on seismic coupling, *Geology*, *25*, 487–490.
- Singh, S. K., and F. Mortera (1991), Source time functions of large Mexican subduction earthquakes, morphology of the Benioff zone, age of the plate, and their tectonic implications, *J. Geophys. Res.*, *96*, 21,487–21,502.
- Singh, S. K., and M. Pardo (1993), Geometry of the Benioff zone and state of stress in the overriding plate in Central Mexico, *Geophys. Res. Lett.*, *20*, 1483–1486.
- Song, T. A., D. V. Helmberger, M. R. Brudzinski, R. W. Clayton, P. Davis, X. Pérez-Campos, and S. K. Singh (2009), Subducting slab ultra-slow velocity layer coincident with silent earthquakes in Southern Mexico, *Science*, *324*, 502–506.
- Soto, G. L., J. F. Ni, S. P. Grand, E. Sandvol, R. W. Valenzuela, M. G. Speziale, J. M. G. González, and T. D. Reyes (2009), Mantle flow in the Rivera-Cocos subduction zone, *Geophys. J. Int.*, *179*, 1004–1012, doi:10.1111/j.1365-246X.2009.04352.x.
- Stubailo, I., C. Beghein, and P. M. Davis (2012), Structure and anisotropy of the Mexico subduction zone based on Rayleigh-wave analysis and implications for the geometry of the Trans-Mexican Volcanic Belt, *J. Geophys. Res.*, *117*, B05303, doi:10.1029/2011JB008631.
- Suckale, J., S. Rondenay, M. Sachpazi, M. Charalampakis, A. Hosa, and L. H. Royden (2009), High-resolution seismic imaging of the Western Hellenic subduction zone using teleseismic scattered waves, *Geophys. J. Int.*, *178*, 775–791.
- ten Brink, U. (2005), Vertical motions of the Puerto Rico Trench and Puerto Rico and their cause, *J. Geophys. Res.*, *110*, B06404, doi:10.1029/2004JB003459.

- Vargas, C. A., and P. Mann (2013), Tearing and breaking off of subducted slabs as the result of collision of the Panama arc-indentor with Northwestern South America, *Bull. Seismol. Soc. Am.*, *103*, 2025–2046, doi:10.1785/0120120328.
- VEOX (2010), Veracruz-Oaxaca subduction experiment, Caltech, dataset, doi:10.7909/C3MW2F2C.
- Verma, S. P. (2006), Extension-related origin of magmas from a garnet-bearing source in the Los Tuxtlas volcanic field, Mexico, *Int. J. Earth Sci.*, *95*, 871–901.
- Wang, K., and S. L. Bilek (2011), Do subducting seamounts generate or stop large earthquakes?, *Geology*, *39*, 819–822, doi:10.1130/G31856.1.
- Wortel, M. J. R., and W. Spakman (2000), Subduction and slab detachment in the Mediterranean-Carpathian Region, *Science*, *290*, 1910–1917.
- Yang, H., Y. Liu, and J. Lin (2013), Geometrical effects of a subducted seamount on stopping megathrust ruptures, *Geophys. Res. Lett.*, *40*, 1–6, doi:10.1002/grl.50509.
- Yang, T., S. P. Grand, D. Wilson, M. Guzman-Speziale, J. M. Gomez-Gonzalez, T. Dominguez-Reyes, and J. Ni (2009), Seismic structure beneath the Rivera subduction zone from finite-frequency seismic tomography, *J. Geophys. Res.*, *114*, B01302, doi:10.1029/2008JB005830.
- Yogodzinski, G. M., J. M. Lees, T. G. Churikova, F. Dorendorf, G. Wöerner, and O. N. Volynets (2001), Geochemical evidence for the melting of subducting oceanic lithosphere at plate edges, *Nature*, *409*, 500–504.
- Zandt, G., and E. Humphreys (2008), Toroidal mantle flow through the western U.S. slab window, *Geology*, *36*, 295–298, doi:10.1130/G24611A.1.
- Zhao, L.-S., and D. V. Helmberger (1994), Source estimation from broadband regional seismograms, *Bull. Seismol. Soc. Am.*, *84*, 91–104.
- Zhu, L., and D. V. Helmberger (1996), Advancement in source estimation techniques using broadband regional seismograms, *Bull. Seismol. Soc. Am.*, *86*, 1634–1641.
- Zoback, M. L. (1992), First- and second-order patterns of stress in the lithosphere: The world stress map project, *J. Geophys. Res.*, *97*, 11,703–11,728.

Erratum

In the originally published version of this article two citations were missing. The error has since been corrected and this version may be considered the authoritative version of record.